Univerzita Karlova v Praze
Přírodovědecká fakulta

DIPLOMOVÁ PRÁCE

Anton Repko

Příprava magnetických a optických nanočástic

Katedra anorganické chemie

Vedoucí diplomové práce: RNDr. Daniel Nižňanský, Ph.D.
Konzultant: Jana Poltierová Vejpravová

Studijní program: Anorganická chemie

2010

Charles University of Prague
Faculty of Science

DIPLOMA THESIS

Anton Repko

Preparation of magnetic and optical nanoparticles

Department of Inorganic Chemistry

Supervisor: RNDr. Daniel Nižňanský, Ph.D.
Consultant: Jana Poltierová Vejpravová

Study program: Inorganic chemistry

2010

I would like to thank to my supervisor RNDr. Daniel Nižňanský, Ph.D. for his professional and technical support. I would also like to thank to Jana Poltierová Vejpravová from Faculty of Mathematics and Physics for measuring magnetic properties and for explaining theory behind it, Jan Valenta from Faculty of Mathematics and Physics for measuring up-conversion luminescence spectra, Jaroslav Kupčík for taking TEM photographs at Institute of Inorganic Chemisty in Řež and Maria del Puerto Morales from Department of Particulate Materials, CSIC, Madrid, Spain where I did large part of work on this thesis.

I declare that I worked out this thesis autonomously, under supervision of RNDr. Daniel Nižňanský, and that I properly cited all used literal sources. I agree with lending of this work and its publication.

In Prague 3.5.2010 Anton Repko

Contents

Název práce: Příprava magnetických a optických nanočástic
Autor: Anton Repko
Katedra: Katedra anorganické chemie, PřF UK Praha
Vedoucí diplomové práce: RNDr. Daniel Nižňanský, Ph.D.
e-mail vedoucího: niznansk@natur.cuni.cz

Abstrakt: V předložené práci studujeme možnosti přípravy magnetických a optických nanočástic hydrotermální metodou. Konkrétně se jedná o přípravu částic feritu kobaltnatého ($CoFe_2O_4$) a fluoridu sodno-yttritého ($NaYF_4$) dopovaného Yb^{3+} a Er^{3+} z příslušných dusičnanů v prostředí voda - ethanol - kyselina olejová a modifikace této metody. Touto metodou je možno připravit částice s úzkou distribucí velikostí (monodisperzní částice). Připravené částice feritu vykazují superparamagnetismus a částice $NaYF_4$ tzv. up-conversion, přeměnu infračerveného záření (980 nm) na viditelné světlo.

Klíčová slova: nanokrystaly, superparamagnetismus, up-conversion, $CoFe_2O_4$, $NaYF_4$, hydrotermální příprava

Title: Preparation of magnetic and optical nanoparticles
Author: Anton Repko
Department: Department of Inorganic Chemistry, Faculty of Science, Charles University of Prague
Supervisor: RNDr. Daniel Nižňanský, Ph.D.
Supervisor's e-mail address: niznansk@natur.cuni.cz

Abstract: In the present work we study methods of preparation of magnetic and optical nanoparticles by hydrothermal method. Specifically, we prepared particles of cobalt ferrite ($CoFe_2O_4$) and sodium yttrium fluoride ($NaYF_4$) doped by Yb^{3+} a Er^{3+} from corresponding nitrates in the system of water - ethanol - oleic acid, and in modified systems. By this method, it is possible to prepare particles of narrow size distribution (monodisperse particles). Prepared particles of ferrite show superparamagnetism and particles of $NaYF_4$ up-conversion, i.e. conversion of infrared (980 nm) to visible light.

Keywords: nanocrystals, superparamagnetism, up-conversion, $CoFe_2O_4$, $NaYF_4$, hydrothermal synthesis

Chapter 1

Introduction

Magnetic nanoparticles have been attracting large attention in last years due to their wide potential application and tunable properties. Small superparamagnetic particles can be used for various biomedical applications ranging form drug delivery, cancer diagnostic and treatment, to various *in vitro* labeling and separation experiments. Larger particles could be used for information storage and in other future electronic devices. Older routes, based mainly on coprecipitation, suffer from poor size distribution, aggregation and low crystallinity. Some problems were solved by reverse micelle approach, but current development is focusing on high-temperature decomposition in organic solvents. This method leads to well crystalline and monodisperse magnetic nanoparticles. [1]

However, this method is not environmental friendly due to toxic organic solvents and by-products, which are difficult to remove from prepared particles. Recently, hydrothermal treatment in fatty acid - water - ethanol system was proposed to lead to high-quality particles of various types (precious metals, dielectric, magnetic, semiconductor, luminescent) [2]. Prepared particles have similar properties as from organic decomposition methods, but don't contain any toxic organic substances. Moreover, this method is environmental friendly and easier to conduct, as it doesn't need special water- and oxygen-free procedures. Despite these advantages, hydrothermal synthesis hasn't been extensively investigated and exploited for magnetic particles so far. In this work, I was trying to understand influence of various factors to improve properties of prepared particles. I have chosen cobalt ferrite ($CoFe_2O_4$) as a model material, which does't show complications connected with oxidation of Fe^{2+} as in magnetite (Fe_3O_4).

Particles of another type widely investigated nowadays are up-conversion particles, mainly $NaYF_4$: Yb^{3+},Er^{3+}, which convert 980 nm infrared radiation to visible light. Although the high efficiency of $NaYF_4$: Yb^{3+},Er^{3+} material was discovered already in 1972 [3], it was not until now, when facile routes were found to prepare it in form of efficient nanoparticles. High-temperature reactions in organic solvents and hydrothermal routes are now being investigated in similar extent. These nanoparticles could find wide application in biological labeling and imaging, and replace now used down-conversion materials, as organic dyes and quantum dots. There are also some other promising applications, like 3D color displays and solid-state lasers [4, 5].

In this work, I investigated phase transition of $NaYF_4$ nanoparticles, its dependence on temperature of treatment, and luminescent properties in comparison with LaF_3. Existence of two phases is main factor which complicates synthesis of $NaYF_4$ material (especially small particles < 20 nm) and hasn't been very well solved for hydrothermal synthesis so far.

Chapter 2

Literature review

2.1 Magnetic particles by organic decomposition

Magnetic nanoparticles of narrow size distribution (i.e. monodisperse particles) are now widely prepared by *organic decomposition* method. This method involves decomposition of organometallic precursor in high-boiling organic solvent at temperatures of about 300 °C. Most frequently prepared nanocrystals are of magnetite Fe_3O_4 (because of its low toxicity in potential biological applications) and other ferrites MFe_2O_4 (where M = Co, Mn etc.). Strategies leading to the particles of good size distribution involve e.g.:

- decomposition of metal acetylacetonates ($Fe(acac)_3$, $Co(acac)_2$) in presence of 1,2-hexadecanediol (or 1,2-dodecanediol; reducing agent), oleic acid and oleylamine (surface capping) in diphenylether (b.p. 265 °C) or dibenzylether (b.p. 265 °C) [1]

- synthesis of $CoFe_2O_4$ by decomposition of iron and cobalt oleates in 1-octadecene, with controlled heating rate and aging time [6]

As reported, the size and shape of the particles is sensitive to careful adjustment of heating rate and duration of the treatment. Alternatively, seed-mediated growth can be used to prepare bigger particles from smaller ones. Prepared particles can be precipitated from reaction mixture by alcohol (e.g. ethanol or isopropanol). They are covered by capping agent (oleate) which make them hydrophobic. They are readily dispersible in non-polar organic solvents (hexane, cyclohexane, toluene etc).

2.2 Magnetic particles by hydrothermal method

Although organic decomposition method leads to particles with very good size distribution, there are several drawbacks: Complicated reaction procedure involving inert atmosphere, temperature control and precursor preparation. Resulting product contains high-boiling organic solvent and other toxic by-products, which are difficult to remove, if the particles are to be used in biomedical applications. Some of the difficulties can be solved by *hydrothermal method*, which was proposed by Wang et al [2]. It involves elevated temperature treatment (up to 200 °C) of the mixture of metal salt, fatty acid, its sodium salt, ethanol and water in autoclave tube (closed system). This method is quite general and can be used for synthesis of various nanocrystals: precious metal (Ag, Au, Pt), magnetic (MFe_2O_4), semiconductor (ZnS, CdSe), fluorescent (doped LaF_3, $NaYF_4$). Prepared nanoparticles are capped with fatty acid and are hydrophobic. They are very similar to particles prepared by organic decomposition, with the advantage of not containing toxic organic residues. Author further develops this method for magnetite particles in [7].

To be used for biomedical applications, prepared magnetic particles need to be made hydrophilic. This can be achieved by ligand exchange, e.g. by 1,2-dimercaptosuccinic acid [8].

2.3 Luminescent particles by organic decomposition

Other important class of particles involves specific optical properties, namely luminescence, caused by irradiation by ultraviolet or infrared radiation (fluorescence, up-conversion). For example, semiconductor particles (quantum dots: ZnS, ZnSe, CdS, CdSe, CdTe, PbS) show luminescence with emission wavelength dependent on the size of the particles. They are commonly prepared by decomposition in organic solvent. Most widely used is the reaction of organic Cd precursor with elemental Se in hot (300 °C) trioctylphosphine (TOPO) [9]. These particles can be prepared also by hydrothermal method [10], but usually show lower photoluminescence.

Advantages of quantum dots are good photostability (compared to organic dyes) and tunability of emission, but there are several drawbacks: high toxicity and exposition to harmful ultraviolet radiation (in biomedical

applications). These problems can be circumvented by up-conversion particles. The most used host materials are $NaYF_4$ and LaF_3. $NaYF_4$ forms two phases: cubic (α) and hexagonal (β). Although β phase is thermodynamically stable at < 700 °C [11] and leads to more efficient up-conversion [12] (especially for small particles), usually α phase is formed first due to kinetic reasons. But recrystallization at higher temperature often leads to large crystallites of desired β phase (see e.g. [16, 25, 26]). LaF_3 forms only hexagonal phase, so small particles can be prepared directly by organic [13] or hydrothermal method [14], but it is less efficient for up-conversion than β-$NaYF_4$.

Recent claims about synthesis of small β-$NaYF_4$ nanoparticles in organic solvents were:

- Yi and Chow (2006) [15] reported synthesis of 10 and 15 nm β-$NaYF_4$ particles by decomposition of trifluoroacetates of Na, Y, Yb, Er/Tm in oleylamine at 330-340 °C. This method was based on previous preparation of LaF_3 nanoplates from $La(CF_3COO)_3$ in oleic acid and octadecene by Yan [13]. Zhang and Yan [16] and Capobianco [17], reported only α-$NaYF_4$ as they used mixture of oleic acid, oleylamine and octadecene as a solvent. Zhang and Yan further improved their method to obtain 20 nm β-$NaYF_4$ by heat treatment of previously prepared α-$NaYF_4$ particles in octadecene with oleic acid and CF_3COONa [18]. Yi an Chow (2007, 2009) [19, 20] further increased up-conversion intensity of their particles up to 15 times by deposition of undoped $NaYF_4$ layer (optimum thickness was 3 nm). Inert layer prevented nonradiative energy transfer to surface molecules and defects.

- To prevent using organic fluorinated compounds, some authors used oleate as lanthanide source and NaF as fluoride source (in solid state during reaction). Chen (2006) [21] used octadecene as a solvent at 260 °C and obtained 35×20 nm hexagonal plates of β-$NaYF_4$.

- Similar method was proposed by Li and Zhang (2008) [22]: reaction of $LnCl_3$, oleic acid, NH_4F and NaOH in octadecene at 300 °C, which led to 20 nm β-$NaYF_4$ nanoparticles. Reduction of size was attributed to the excess of oleic acid.

- Chen (2008) [23] improved his method by addition of oleic acid to his reaction and obtainted spherical particles of 20-45 nm. Size was controlled by NaF content (more NaF – smaller particles).

- Schäfer (2009) [24] reported direct synthesis of β-$NaYF_4$ from $Ln_2(CO_3)_3$ and NH_4F in oleylamine at 55 °C or even in solid state at room temperature. However, size distribution was not very good and post-heat treatment was needed to obtain good up-conversion luminescence (although dispersibility was mantained and the size was 20 nm).

2.4 Luminescent particles by hydrothermal methods

Particles of $NaYF_4$ prepared by hydrothermal method using oleic acid are either small, but with inefficient up-conversion (α phase – cubic), or in the form of desired β phase, but with oversized dimensions (100 nm to 1 μm) – this is caused by recrystallization of previously formed α phase – therefore prolonged reaction time is necessary (24 h) [25, 26]. Clearly dispersible hydrophobic particles prepared by hydrothermal method (using oleic acid) are always of α-phase. There are some reports on smaller hydrophilic particles of β-phase prepared by hydro/solvo-thermal methods:

- 40 nm particles prepared from Ln stearates and NaF in water-ethanol solution in the presence of water soluble polymer (polyethylene glycol, polyvinylpyrrolidone, polyacrylic acid or polyethyleneimine) [27].
- 50 nm particles by the reaction of Ln nitrates, NaF in ethanol in the presence of EDTA reported by Li (2005) [28], but no clear procedure was given. Same author further utilizes similar particles (prepared in glycol) to obtain FRET (fluorescence resonant energy transfer) biosensor based on quenching of the luminescence by gold nanoparticles [29].
- 55 nm polycrystalline particles (23 nm crystallites by XRD) prepared by the reaction of NaCl and Ln nitrates within the ionic liquid 1-butyl-3-methylimidazolium tetrafluoroborate in closed autoclave [30].
- Small hydrophobic nanorods (< 50 nm) were prepared by co-doping Gd^{3+} during the hydrothermal synthesis in ethanol - oleic acid - oleate. Gd^{3+} ion facilitated phase transition at lower temperatures and thus led to smaller particles. It didn't affect up-conversion efficiency due to high energy (32200 cm^{-1}) of its first excited state ($^8S_{7/2} \rightarrow {}^6P_{7/2}$) [5]. Small hydrophilic particles covered by polyethyleneimene and doped with Gd^{3+} were directly prepared also by other authors [31].

Chapter 3

Theoretical part

3.1 Magnetic properties

Electromagnetic field is one of the fundamental fields in nature and is described by Maxwell equations. Magnetic field is described by two quantities: magnetic field strength $\vec{H}$ (unit: ampere/meter), which is found in Ampère's law descibing generation of magnetic field from electric currents (and variating electric field, as was added by Maxwell), and magnetic induction $\vec{B}$ (unit: tesla [T]) which is found in Faraday law of electromagnetic induction (generation of electric field by variating magnetic field). These two quantities are not independent, but there are material relations connecting them:

$$\vec{B} = \mu_0(\vec{M} + \vec{H}) \qquad \vec{M} = \chi\vec{H} \tag{3.1}$$

where $\mu_0 = 4\pi \cdot 10^{-7}$ kg.m.s^{-2}.A^{-2} (or m.T/A) is vacuum permeability, $\vec{M}$ is magnetization (0 in vacuum) and χ is magnetic susceptibility of given material. In case of magnetically anisotropic material, χ is tensor, and $\vec{H}$ and $\vec{M}$ can have different directions.

3.1.1 Units

Sample with magnetization $\vec{M}$ and volume V can be described to have magnetic moment $\vec{\mu}$ [A.m^2]:

$$\vec{\mu} = \vec{M}V = \mu_0\chi V\vec{H} = \mu_0\chi_{\mathrm{m}}n\vec{H} = \mu_0\chi_{\mathrm{g}}m\vec{H} \tag{3.2}$$

where χ can be considered as volume susceptibility in contrast to molar susceptibility χ_{m} (n is molar amount) and mass susceptibility χ_{g} (m is mass).

In older literature, the CGS unit system is used, with "emu" as a unit of magnetic moment [32] and other related units:

$$\begin{array}{ll} \mu: & 1\ \mathrm{A.m^2} = 10^3\ \mathrm{emu} \\ M: & 1\ \mathrm{A.m^{-1}} = 10^{-3}\ \mathrm{emu/cm^3} \\ H: & 1\ \mathrm{A.m^{-1}} = 4\pi \cdot 10^{-3}\ \mathrm{Oe} \\ B: & 1\ \mathrm{T} = 10^4\ \mathrm{G} \end{array} \tag{3.3}$$

One gauss (G) and one oersted (Oe) describe the same magnetic field in vacuum. However, in CGS system, unit of magnetization, emu/cm^3 and unit of magnetic field strength, Oe are considered to be of the same dimension and this leads to different numeric value of susceptibility in both systems: $\chi_{\mathrm{SI}} = 4\pi\chi_{\mathrm{CGS}}$.

3.1.2 Diamagnetism

Description of interaction of charged particles with electromagnetic field in theoretical and quantum mechanics can be most easily obtained by subsitution for particle momentum ([33], p.652): $\vec{p} \mapsto \vec{p} - e\vec{A}$, where e is charge of the particle and $\vec{A}$ is vector potential ($\vec{B} = \mathrm{rot}\ \vec{A}$). After substitution, the resulting hamiltonian has the form:

$$\hat{\mathcal{H}} = \frac{(\vec{\hat{p}} - e\vec{A})^2}{2m} = \frac{\hat{p}^2}{2m} - e\frac{\vec{\hat{p}}\cdot\vec{A} + \vec{A}\cdot\vec{\hat{p}}}{2m} + \frac{e^2A^2}{2m} \tag{3.4}$$

Homogeneous magnetic field B in z-direction can be descibed by vector potential $\vec{A} = (-\frac{1}{2}yB, \frac{1}{2}xB, 0)$. In this case, the hamiltonian becomes ([33], p.419):

$$\hat{\mathcal{H}} = -\frac{\hbar^2}{2m}\nabla^2 + \frac{\mathrm{i}e\hbar B}{2m}\left(x\frac{\partial}{\partial y} - y\frac{\partial}{\partial x}\right) + \frac{e^2B^2(x^2+y^2)}{8m} \tag{3.5}$$

First term describes electron free motion, the second interaction of orbital momentum ($\hat{L}_z = -\mathrm{i}\hbar(x\frac{\partial}{\partial y} - y\frac{\partial}{\partial x})$) with the magnetic field $B = \mu_0 H$ and the last term describes the diamagnetism. When electron is moving sphericaly, its mean quadratic distance from nucleus is $\langle r^2\rangle = \langle x^2+y^2+z^2\rangle = \frac{3}{2}\langle x^2+y^2\rangle$. We can extract experssion for the induced magnetic moment and susceptibility from the expression for the total energy (3.5) using $\mathrm{d}E = -VM\mu_0\,\mathrm{d}H$ and $M = \chi H$ to obtain:

$$\chi = -\frac{1}{\mu_0 VH}\frac{\partial E}{\partial H} = -\frac{NZ}{\mu_0 V}\frac{\partial}{\partial H}\left(\frac{e^2\mu_0^2H^2\langle x^2+y^2\rangle}{8m}\right) = -\frac{NZe^2\mu_0\langle r^2\rangle}{6Vm} \tag{3.6}$$

where Z is number of electrons per atom and N is number of atoms per volume V.

In relativistic description of electrons, we obtain term for spin similar to orbital momentum. When electrons are paired and the orbitals are fully occupied, the orbital and the spin momentum are zero and only the diamagnetic term remains. It is the case of a *diamagnetic* material, in which electrons are creating small magnetic moments opposite to the external field.

3.1.3 Paramagnetism

Electron has magnetic moment, $\vec{\mu}$ with spin and orbital contribution (the magnetic and angular moment, respectively, is considered as operator). It is proportional to spin $\vec{S}$ and orbital moment $\vec{L}$:

$$\vec{\mu}_{ls} = -g_s\vec{S}\mu_B - g_l\vec{L}\mu_B \tag{3.7}$$

where minus sign reflects negative charge of electron, $\mu_B = \frac{e\hbar}{2m_e}$ is Bohr magneton, $g_s = 2.0023$ is spin g-factor (calculated from quantum electrodynamics) and $g_l = 1$ for orbital moment. As magnetic moment doesn't have the same direction as angular momentum, observed magnetic moment $\vec{\mu}$ is projection of $\vec{\mu}_{ls}$ to direction of total angular momentum $\vec{J} = \vec{L} + \vec{S}$ due to angular momentum conservation (the same rule is used for estimation of nuclear magnetic moments [34], p.68):

$$\begin{aligned}
\vec{\mu} &= -\frac{\vec{\mu}_{ls}\cdot\vec{J}}{\vec{J}\cdot\vec{J}}\mu_B\vec{J} = -\frac{2.023\,\vec{S}\cdot\vec{S} + (2.023+1)\vec{L}\cdot\vec{S} + \vec{L}\cdot\vec{L}}{J(J+1)}\mu_B\vec{J} \\
&= -\frac{3.023\,J(J+1) + L(L+1) + 3.046\,S(S+1)}{2J(J+1)}\mu_B\vec{J} \\
&= -g\mu_B\vec{J}
\end{aligned} \tag{3.8}$$

where $\vec{L}\cdot\vec{S} = \frac{1}{2}(\vec{J}\cdot\vec{J} - \vec{L}\cdot\vec{L} - \vec{S}\cdot\vec{S}) = \frac{1}{2}(J(J+1) - L(L+1) - S(S+1))$ has been used. As can be seen from previous derivation, overall electron g-factor can be calculated from Landé equation:

$$g \approx 1 + \frac{J(J+1) - L(L+1) + S(S+1)}{2J(J+1)} \tag{3.9}$$

Magnetic moment of the whole atom or ion with unpaired electrons can be calculated by the same Landé equation considering the L–S coupling.

Atoms with non-zero magnetic moment interact with external magnetic field and their energy levels are split: $E = -\vec{\mu} \cdot \vec{B} = -m_J g \mu_B B$, where m_J is projection of total angular momentum, J to the direction of magnetic field. Energy levels are occupied according to Boltzman distribution ($N_i/N = \exp(-\frac{E_i}{k_\mathrm{B}T}) / \sum_j \exp(-\frac{E_j}{k_\mathrm{B}T})$) and average magnetic moment of these atoms contributes to overall magnetic moment of the sample. For the simple two-level system ($J = \frac{1}{2}$, $E = \mp \mu B$), the total magnetic moment of N atoms with magnetic moment μ (without spin-spin interactions) in magnetic field B is ([33], p.421):

$$\mu_N = \frac{N_\uparrow - N_\downarrow}{N_\uparrow + N_\downarrow} N\mu = \frac{\mathrm{e}^{\frac{\mu B}{k_\mathrm{B}T}} - \mathrm{e}^{-\frac{\mu B}{k_\mathrm{B}T}}}{\mathrm{e}^{\frac{\mu B}{k_\mathrm{B}T}} + \mathrm{e}^{-\frac{\mu B}{k_\mathrm{B}T}}} N\mu = N\mu \tanh \frac{\mu B}{k_\mathrm{B}T} \approx \frac{N\mu^2 B}{k_\mathrm{B}T} \quad (3.10)$$

Atoms with higher magnetic moments have more energy levels, but the obtained result for the weak field approximation (Curie law) is similar [33], p.422:

$$\chi = \frac{N}{V} \frac{J(J+1) g^2 \mu_B^2}{3 k_\mathrm{B} T} = \frac{N}{V} \frac{p^2 \mu_B^2}{3 k_\mathrm{B} T} = \frac{C}{T} \quad (3.11)$$

where $p = g\sqrt{J(J+1)}$ is effective number of Bohr magnetons and C is Curie constant. For elements filling $3d$ orbital, better agreement with experimental data is obtained for $p = 2\sqrt{S(S+1)}$. This can be explained by crystal field splitting of ${}^{2S+1}L_J$ terms and quenching of the orbital moment [33], p.426.

When all electrons are paired in atom or ion in ground state $|0\rangle$, but there is an excited state $|s\rangle$ with non-zero matrix element of magnetic dipole moment operator $\langle s|\hat{\mu}_z|0\rangle$, new ground state in non-zero magnetic field B will be mixture of $|0\rangle$ and $|s\rangle$ and will have non-zero magnetic moment. The created magnetic moment will be proportional to the applied magnetic field independently of temperature, what is called *Van Vleck paramagnetism*. This will be valid only for temperature range, where occupation of $|s\rangle$ state is negligible. At higher temperatures, Curie-like behaviour is obtained [33], p.430.

In case of metals, electrons occupy energy levels in conduction band up to Fermi energy, ϵ_F. When no magnetic field is applied, total magnetic moment is zero. When the field is applied, energy levels of electrons with parallel spin orientation are shifted down and energy levels for electrons with antiparallel spin orientation are shifted up. To reach equilibrium, fraction $\frac{\mu B}{\epsilon_F}$ of electrons with antiparallel orientation and in high energy levels will turn over and creates non-zero overall magnetic moment proportional to applied

field B and independent of temperature. This is called *Pauli paramagnetism* of metals. It is valid only for temperatures $k_{\mathrm{B}}T \ll \epsilon_F$ [33], p.435.

3.1.4 Ferromagnetism

When interactions between magnetic moments are sufficiently high, spontaneous ordering occurs below the Curie temperature T_c. However, dipole-dipole interactions are not strong enough (0.1 T induced by Fe atom in neighboring lattice point), and another interaction corresponding to 1000 T is observed for iron [33], p.444. This can be explained by energy of spin-spin interaction [33], p.446:

$$U = -2J\vec{S}_i \cdot \vec{S}_j \tag{3.12}$$

where J is the so-called exchange integral and it is proportional to overlap of the charge distribution at atoms i and j. It has origin in antisymmetrization of the total wave-function of electrons (by Slater determinant; electrons are fermions).

For positive J, magnetic moments prefer parallel alignment, and this leads to *ferromagnetic* behaviour (e.g. Fe, Co, Ni). For temperatures $T > T_c$, thermal motion overcomes spontaneous ordering, and the resulting paramagnetic behaviour can be described by Curie-Weiss law [33], p.444:

$$\chi = \frac{C}{T - T_c} \tag{3.13}$$

Ferromagnetic crystals usually prefer one of crystalographic axes for direction of spontaneous magnetization due to energy minimization. It is called direction of easy magnetization. Energy needed for reorientation to other direction is called *magnetocrystalline* or *anisotropy energy*, K [33], p.471. Its exact definition depends on crystal structure and decription of the axis direction (angles, unit vector coordinates).

Magnetic moments in ferromagnetic materials are arranged in small regions called *domains*, each with distinct orientation of magnetization. This is caused by minimization of energy of magnetic field in surrounding free space ($E \sim \int B^2 \mathrm{d}V$). Boundaries between domains are called *Bloch walls* and they are composed of several layers of atoms with continually changing direction of magnetic moment. Their thickness is limited by anisotropy energy. Size of domains is limited from below by the same reason [33], p. 468–473.

External magnetic field causes movement of Bloch walls and reorientation of moments. Ferromagnetic material then shows non-zero overall magnetic

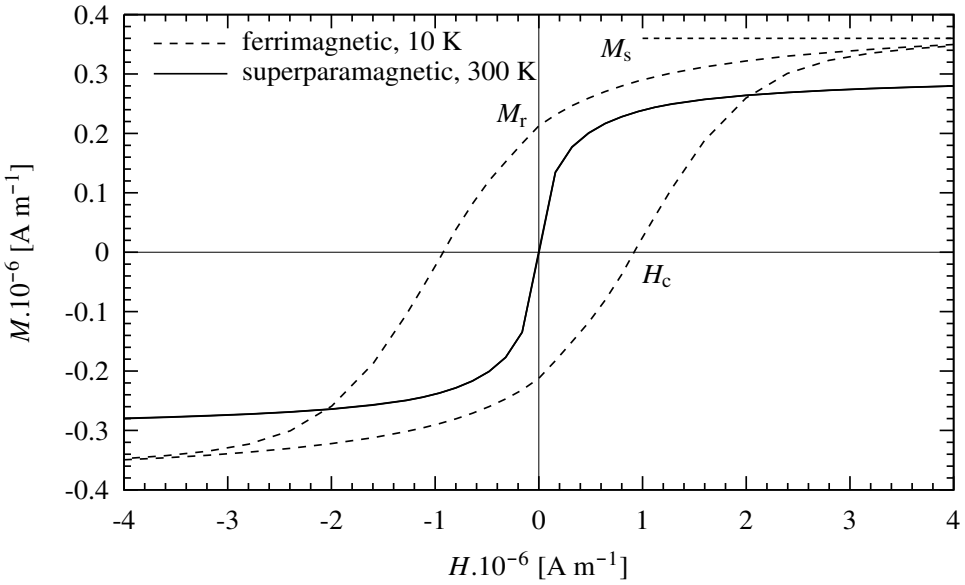

Figure 3.1: Hysteresis loop of 6 nm nanoparticles of $CoFe_2O_4$ at 10 K and 300 K. Depending on temperature, they show either ferromagnetic-like or superparamagnetic behaviour. Coercitive field H_c, remanent magnetization M_r and saturation magnetization M_s is shown.

moment. Dependence of magnetization, M on magnetic field intensity, H is called hysteresis loop (figure 3.1 at 10 K). Important parameters of hysteresis loop are coercitive field H_c, remanent magnetization M_r and saturation magnetization M_s. Inner area of the loop is proportional to the density of energy, which is converted to heat during the full magnetization cycle.

When the particles of ferromagnetic material are sufficiently small, no Bloch walls can form and the particle contains only one domain (figure 3.2). Thus permanent magnets are often prepared by sintering of small particles, because movement of Bloch walls through particle boundaries and subsequent demagnetization is suppressed [33], p. 476–477.

3.1.5 Ferrimagnetism and antiferromagnetism

Some types of materials have two types of crystallographic sites occupied by atoms with non-zero magnetic moments and negative exchange integral (most notably ferrites, MFe_2O_4). Two sublattices are formed with opposite direction of magnetic moments (figure 3.3). In case of *ferrimagnetism*, they are not entirely compensated, but in case of *antiferromagnetism* they are.

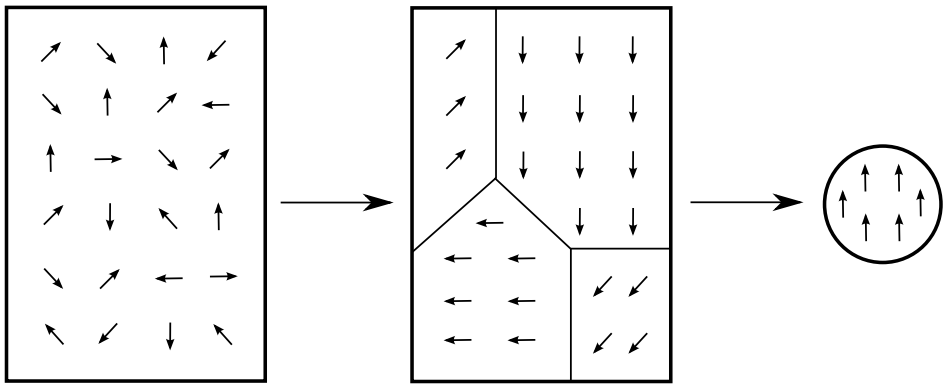

Figure 3.2: Paramagnetic material, multi-domain ferromagnet and single-domain particle.

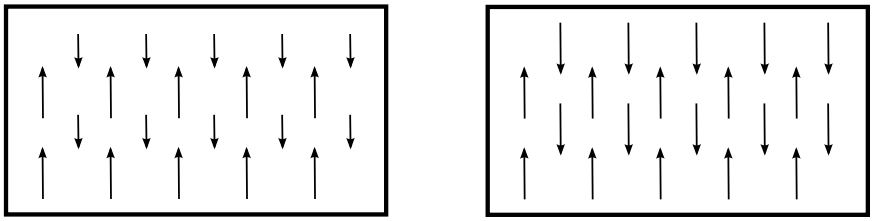

Figure 3.3: Ferrimagnetic material (left) and antiferromagnetic material (right).

The paramagnetic behaviour over the Curie temperature (or Néel temperature T_N for antiferromagnets) can be approximately described by Curie-Weiss law (3.13), with "$-\,T_c$" replaced by "$+\,\theta$" for antiferromagnets (usually $\theta > T_\mathrm{N}$) [33], p. 458–466.

3.1.6 Superparamagnetism

Monodomain particles with anisotropy energy K have fixed orientation of the magnetization in easy axis at low temperatures – this is called *blocked state*. Energy needed to reorientation of magnetic moment of whole particle (with cubic symmetry) is:

$$E_A = KV \sin^2 \theta \tag{3.14}$$

where V is volume of the particle and θ is angle between easy axis and magnetization direction. When $k_\mathrm{B}T$ becomes comparable to E_A, the parti-

cle becomes *superparamagnetic* and its magnetization is randomly flipping. System composed of such particles will behave like paramagnet with high susceptibility, where particles with their moments play role of atoms in usual paramagnet. Blocking temperature T_{B}, where transition from the blocked state to the superparamagnetic state occurs, depends on the time scale of measurement by the Néel equation:

$$\tau = \tau_0 \, \mathrm{e}^{KV/k_{\mathrm{B}}T} \tag{3.15}$$

where τ_0 is the characteristic relaxation time. For Mössbauer spectroscopy, it is around 10-100 ns. [35]

One of methods how to obtain the blocking temperature, is measurement of magnetization during zero-field-cooling (ZFC) and field-cooling (FC). Sample is put into magnetometer and cooled under zero magnetic field. Then, small field is turned on (e.g. 5 mT), and sample is slowly heated and its magnetization is recorded (ZFC curve). Then it is again cooled, but with magnetic field turned on. During heating, FC curve is recorded. ZFC curve shows peak at temperature T_{B1} when majority of particles are unblocked and become superparamagnetic (see figure 5.14 in chapter Results). ZFC and FC curves join at temperature T_{B2} when all particles are superparamagnetic. Above the T_{B2} both curves decrease as C/T according to Curie law for paramagnets (3.11). [36]

3.2 Mössbauer spectroscopy

Nucleus ^{57}Fe ($I^\pi = 1/2^-$), with natural isotopic abundance 2.2%, has some fortuitous properties which can be utilized for non-destructive investigation of chemical and magnetic state of iron atoms in solids. It has excited state at 14.413 keV with spin and parity $I^\pi = 3/2^-$ and mean life $\tau = 142$ ns (half life is: $T_{1/2} = \tau \cdot \ln 2 = 98.3$ ns). It is produced in 9.2% of decays of radioactive ^{57}Co with half life 271.8 days. [37]

During the absorption and emission of photon by free atom, some energy is lost due to momentum conservation (photon carries momentum $p = E_\gamma/c$):

$$\Delta E_{\mathrm{free}} = \frac{p^2}{2m_{\mathrm{Fe}}} = \frac{E_\gamma^2}{2m_{\mathrm{Fe}}c^2} = \frac{(0.014413\ \mathrm{MeV})^2}{2 \cdot 57 \cdot 931.5\ \mathrm{MeV}} \approx 1.96{\cdot}10^{-3}\ \mathrm{eV} = 1.36{\cdot}10^{-7} E_\gamma \tag{3.16}$$

But in crystal lattice, this energy is usually not sufficient for phonon excitation, so photon is emitted and absorbed without energy loss, and resonant absorption of emitted photon by other ^{57}Fe nucleus is possible.

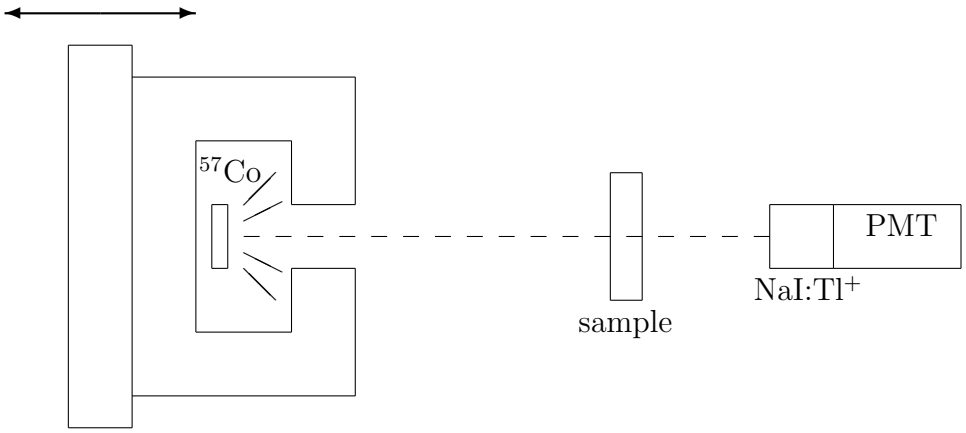

Figure 3.4: Scheme of arrangement for the measurement of Mössbauer effect. γ photons are emitted from ^{57}Co embedded in stainless steel and placed on moving support. After going through the sample, they are detected in scintillator coupled with photomultiplier tube and analog-digital converters.

Mössbauer spectroscopy utilizes resonant absorption of 14.413 keV photons (produced indirectly from ^{57}Co) by ^{57}Fe nuclei in the sample (this method is also used for some other nuclei). Full width at half maximum (FWHM), Γ of the emission and absorption peak in γ energy distribution can be calculated from the mean life: $\Gamma = \hbar/\tau = 4.6 \cdot 10^{-9}$ eV $= 3.2 \cdot 10^{-13} E_\gamma$ [34], p.79. Peaks have Lorentz distribution $\frac{\Gamma^2}{((E-E_0)^2+\Gamma^2/4}$ (Fourier transformed decay law $\exp(-t/\tau)$) [34], p.246. Final spectrum is obtained as a number of photons which were not absorbed by the sample. It is convolution of emission and absorption distribution, which is again Lorentzian, but with double width (Fourier transform of squared decay law):

$$N(E_\gamma) = N_0(E_\gamma) - \frac{\Gamma^2}{(E_\gamma - E_0)^2 + \Gamma^2} \cdot x \tag{3.17}$$

where x is some small constant proportional to the amount of sample (x shoud be small for this equation to be valid). The energy of photons is adjusted by Doppler shift, moving the emitter with constant acceleration, and so energy is plotted in units mm/s (figure 3.4) [34], p. 116–117.

Ground energy level of ^{57}Fe nucleus has non-zero spin ($I^\pi = 1/2^-$) and magnetic moment, so this energy level is split in magnetic field. Excited state at 14.413 keV has even higher spin ($I^\pi = 3/2^-$), and it has also electric

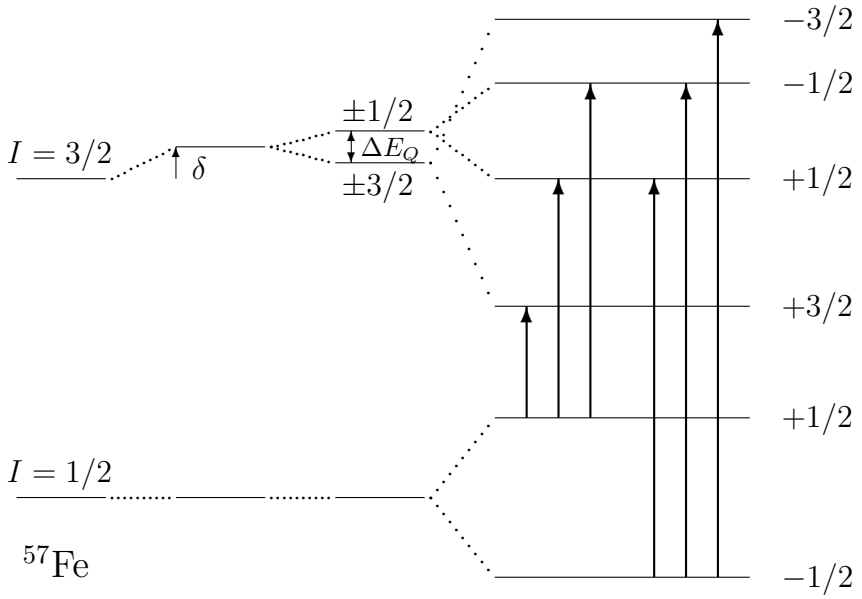

Figure 3.5: Energy level scheme of ^{57}Fe and its excited state in changed electron density (isomer shift, δ), inhomogeneous electric field (quadrupole splitting, ΔE_Q) and magnetic field B

quadrupole moment – this energy level is further split in non-homogeneous electric field.

For iron (or ^{57}Co precursor) incorporated in stainless steel or rhodium, there is no inhomogeneous electric field nor magnetic field acting on ^{57}Fe nucleus, so energy levels are not split and monoenergetic γ photons are produced (not counting Lorentz distribution and 122 keV photons which are excluded by their large signal from photomultiplier tube). There are three parameters, which can be obtained from position and number of peaks in measured distribution:

- Isomer shift δ [mm/s], indicating position of the center of multiplet relative to α-Fe standard. It is related to electron density at nucleus of ^{57}Fe, which is most affected by oxidation state of iron, e.g. Fe^{2+} has $\delta \approx 0.8 - 1.2$ and Fe^{3+} has $\delta \approx 0.3 - 0.5$. [38]

- Quadrupole splitting ΔE_Q [mm/s], indicating inhomogeneity of electric field at the nucleus. It is characteristic for each type of material.

- Non-zero magnetic field B, which causes splitting to the sextet. This

splitting only appears, when field B is stable at least for the time of mean-life of $^{57}Fe^*$ (ca. 100 ns; characteristic time-resolution of Mössbauer spectroscopy).

Obtained spectrum is fitted with multiple Lorentz distributions with suitably constrained parameters. Isomer shift, quadrupole splitting and magnetic field are obtained for each group of chemically equivalent atoms of Fe in investigated solid sample.

3.3 Light scattering

Two important parameters were investigated on Malvern Zetasizer instrument: hydrodynamic size and zeta potential of the particles. It utilizes scattering of red laser light (633 nm) for determination of these parameters. Following theory is based on explanation found in User Manual shipped with this instrument [39].

3.3.1 Dynamic light scattering

Particles dispersed in liquid have different refractive index than solvent. Light is being scattered on them, and can be observed by focusing detector on the light trace created by laser in investigated solution. Although the amount of scattered light is quantity strongly dependent on the size of particles, only fluctuations in light scattering intensity are used to measure their size. Particles are moving randomly in solvent, what is called *Brownian motion*. Its speed is dependent on particle size, temperature and viscosity of solvent. Small particles move quickly and large ones slowly. Velocity of the particles is obtained from rate of fluctuations of scattered light. This can be quantitatively described using autocorrelation function (it is also used in many other fields):

$$G(t) = \frac{\int f(\tau + t) f(\tau) \mathrm{d}\tau}{\int f(\tau)^2 \mathrm{d}\tau} \tag{3.18}$$

Here, $f(t)$ is intensity of scattered light (backscattered at 173° in Zetasizer) as a function of time, usually shifted down by average value to get $\int f(t)\mathrm{d}t = 0$. $G(t)$ then quantifies amount of correlation between two measurements separated in time by t. $G(t = 0)$ is 1 and slowly approaches 0 for increasing t.

Correlation function is then used to obtain size distribution. Zetasizer software does fitting with functions known from calibration with well defined particles of latex of very narrow size distribution. By this method *intensity* distribution is obtained. It tells how much light was scattered by particles of given sizes. Usually, we want to obtain *number* or *volume* distribution. Number distribution is simply number of particles for given sizes. Volume distribution is the number distribution weighted (i.e. multiplied) by volume (r^3), so more weight is given to larger particles. From Rayleigh's approximation, intensity of scattered light is proportional to r^6. So even more weight is given to larger particles in intensity distribution. If we have sample with 5 nm particles and 0.1% (by number) of 50 nm particles, in intensity distribution 50 nm particles will be 1000 times more intense than 5 nm particles. Thus, for accurate measurements, larger particles and dust should be avoided.

3.3.2 Zeta potential measurement

Charged particles in solution attract ions of opposite charge and polarize solvent molecules. When the particle moves, certain amount of attracted ions and molecules moves with it. Layer separating them from bulk solution is called *slipping plane*. Electrostatic potential at this layer is called *zeta potential*. Zeta potential is affected mainly by pH. Particles with large positive or negative zeta potential (≥ 30 mV) are usually stable in colloidal dispersion. Value of pH, for which zeta potential is zero, is called *isoelectric point*. At this point, dispersion is not stable and particles tend to flocculate.

When electric field E is applied, charged particles move with velocity v given by the equilibrium of electric force and viscous force. *Electrophoretic mobility* $\mu_e = \frac{v}{E}$ can be calculated from Henry's equation:

$$\mu_e = \frac{2\varepsilon\zeta f(Ka)}{3\eta} \tag{3.19}$$

where ε is permitivity (dielectric constant), ζ is zeta potential, η is viscosity and $f(Ka)$ is Henry's function usually approximated by:

a) 1.5 in Smoluchowski approximation: for particles > 0.2 μm dispersed in electrolyte containing $> 10^{-3}$ M salt.

b) 1.0 in Huckel approximation: for small particles in media with low permitivity.

Velocity of particles can be obtained by *laser Doppler velocimetry*. Laser light scattered at 13° is combined with reference beam. Wavelength of the light scattered by moving particles is changed by Doppler shift and this small effect is measured by time dependent interference with reference beam. Newer arrangement used in Zetasizer measures phase shift instead of time dependent interference. This impoves speed and resolution.

In classical arrangement, there is a problem with flow of solvent near the charged cell walls (flow in the center of the cell is then in opposite direction). Zetasizer combines fast field reversal, when flow of solvent is suppressed, to obtain mean zeta potential, and slow field reversal to obtain distribution with higher resolution – systematic shift is then corrected by fast field reversal measurement.

3.4 Up-conversion luminescence

Up-conversion is a process in which two (or more) lower energy photons are absorbed and one higher energy photon is emitted, usually with less than twofold frequency, in contrast with second harmonic generation. It consist of energy transfer from one excited ion (sensitizer) to another already-excited ion (activator). Energy transfer can be nonradiative or multiphonon-assisted. This process was discovered by Auzel in 1966 who gave recent review about it in [40]. Two most frequently used dopant combinations are Yb^{3+}–Er^{3+} (red and green emission) and Yb^{3+}–Tm^{3+} (NIR and blue emission). The process

Table 3.1: Experimental energy levels (centers of gravity) of Er^{3+} [41], Tm^{3+} [42], Yb^{3+} [43] in LaF_3.

ion	state	energy	
		[eV]	[cm^{-1}]
Er^{3+}	$^4I_{15/2}$	0	0
	$^4I_{13/2}$	0.804	6481
	$^4I_{11/2}$	1.255	10123
	$^4I_{9/2}$	1.531	12351
	$^4F_{9/2}$	1.889	15236
	$^4S_{3/2}$	2.275	18353
	$^2H_{11/2}$	2.370	19118
	$^4F_{7/2}$	2.541	20492
	$^4F_{5/2}$	2.748	22162
	$^4F_{3/2}$	2.789	22494

ion	state	energy	
		[eV]	[cm^{-1}]
Tm^{3+}	$^3H_6$	0	0
	$^3F_4$	0.714	5758
	$^3H_5$	1.021	8236
	$^3H_4$	1.564	12611
	$^3F_3$	1.793	14459
	$^3F_2$	1.869	15073
	$^1G_4$	2.635	21252
Yb^{3+}	$^2F_{7/2}$	0	0
	$^2F_{5/2}$	1.272	10260

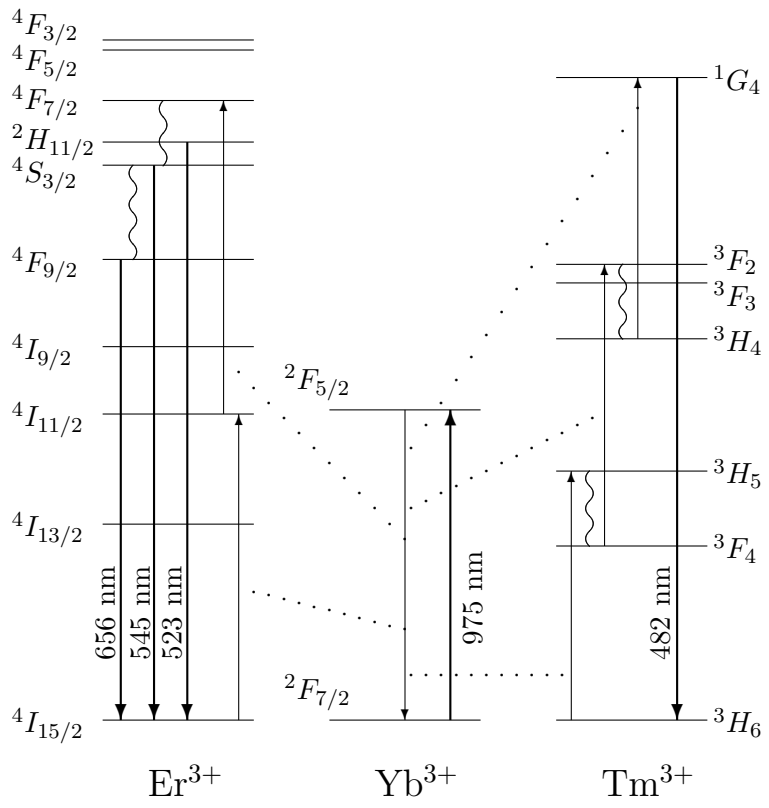

Figure 3.6: Energy level diagram for Er^{3+}, Tm^{3+}, Yb^{3+} showing processes involved in up-conversion (full arrow: radiative process, wavy line: multi-phonon relaxation, thin arrow and dotted lines: energy transfer).

starts with absorption of 980 nm photons in Yb^{3+} ions, which then transfer energy multiple times to Er^{3+} or Tm^{3+}, which emit photon with higher energy (usually after some non-radiative relaxation). The energy levels for Yb^{3+}, Er^{3+} and Tm^{3+} in LaF_3 are given in table 3.1 and figure 3.6. They are further split by crystal field; full width is usually around 200 cm^{-1} or 0.025 eV, so only center-of-gravity values are shown.

Radiative transitions $4f - 4f$ are relatively slow. This on one side makes possible energy transfer between Ln^{3+} ions, on other side provides time for non-radiative deexcitation which is not usually wanted. Non-radiative mul-

tiphonon relaxation rate between two adjacent energy levels is [4]:

$$k_{\mathrm{nr}} \sim \exp(-\beta \frac{\Delta E}{\hbar \omega_{\max}}) \tag{3.20}$$

where β is empirical constant, ΔE is energy difference between adjacent energy levels and $\hbar\omega_{\max}$ is highest-energy vibrational mode of the host lattice. For efficient up-conversion and other optical applications, it is important to have sufficiently separated energy levels in dopant ion (e.g. Er^{3+}, Tm^{3+}, Yb^{3+}) and host lattice with low phonon energies (halides, but only fluorides are not soluble in water).

One of the most efficient host materials is β-phase (hexagonal) of $NaYF_4$ doped with about 20% Yb^{3+} and 2% Er^{3+} or 0.3% Tm^{3+}. It's efficiency for green emission is 10 times larger than of α-phase (cubic) [12]. High efficiency is attributed to favorable crystal field around Yb^{3+} and Er^{3+} ions (enabling resonant energy transfer) and low phonon energies [44].

Structure of α-$NaYF_4$ is of fluorite type ($F\,m\bar{3}m$), where Na^+ and Y^{3+} ions are arranged in face-centered-cubic lattice (with random distribution) and F^- ions occupy tetrahedral positions. Cell parameter is $a = 5.499$ Å [11]. Structure of β-$NaYF_4$ can be related to UCl_3 structure ($C\,6_3/m$, [45]) where each U^{3+} ion is surrounded by six Cl^- ions arranged in trigonal prism, and other three Cl^- capping sides of the prism. But β-$NaYF_4$ (better $Na_{1.5}Y_{1.5}F_6$) has less symetric structure with $P\,\bar{6}$ symmetry (#174). Lattice paremeters are $a = 5.973$ Å, $c = 3.528$ Å. There are 3 sites occupied by cations [46]:

- site $1a$, occupied by Y^{3+}, forming skeleton of primitive hexagonal lattice; nine-fold coordinated by F^- as in UCl_3
- site $1f$, occupied randomly by $\frac{1}{2}Na^+$ and $\frac{1}{2}Y^{3+}$; nine-fold coordinated by F^-
- site $2h$, occupied randomly by $\frac{1}{2}Na^+$ and vacancies; six-fold coordinated by F^-

It should be noted, that three F^- capping the sides of the prism $1a$ are at vertices of prisms $1f$ and vice versa.

Chapter 4

Experimental part

I focused on the preparation of:

- $CoFe_2O_4$: particles with high magnetic anisotropy and, in contrast with Fe_3O_4, stable against oxidation
- $NaYF_4$ doped with Er^{3+} and Yb^{3+}: up-conversion particles converting 980 nm near-infrared into visible red and green light
- hydrophilic $CoFe_2O_4$ by substitution of oleic acid on as-prepared particles by 2,3-dimercaptosuccinic acid (DMSA)

4.1 Characterization methods

Characterization of the samples was done by following methods:

- Elemental composition (Fe, Co content) of hexane dispersions of magnetic particles was measured (after 50 μl of hexane dispersion was dried, digested with HNO_3 and HCl and diluted to 50 ml by water) using plasma emission spectrometer (ICP), PERKIN ELMER OPTIMA 2100 DV at Instituto de Ciencia de Materiales de Madrid, CSIC, Madrid.
- Transmission electron microscopy was carried out on 200 keV JEOL-2000 FXII at ICMM, CSIC, Madrid. Hydrophobic samples were diluted with hexane and a drop of this dispersion was dried on copper grid. Hydrophilic samples in water were diluted by ethanol and a drop of this dispersion was dried on copper grid. Copper grids had been coated

with polymer and carbon. All pictures of $CoFe_2O_4$ particles were taken at magnification 200k. Pictures on figure 5.21 were taken on microscope Philips 201 (80 kV) at Institute of Inorganic Chemistry AS CR in Řež.

- Powder X-ray diffraction was carried out on PANalytical X'Pert PRO using Cu K_α radiation with secondary monochromator and PIXcel detector at Faculty of Natural Sciences, Charles University, Prague. Samples were dried (in case of hexane dispersion) or spread as a powder (sediments) on glass plate. Step was 0.039° and slits were 0.25° and 0.5°. Profile analysis to obtain particle size was done by FullProf WinPLOTR [May 2009]. Instrument resolution function was obtained using LaB_6 powder and step 0.007°.

- Magnetic measurements: zero-field-cooled (ZFC) and field-cooled (FC) magnetizations (applied field 5 mT) and hysteresis curves at various temperatures were measured on Quantum Design MPMS7XL and PPMS9 device (SQUID) at Joint Laboratory for Magnetic Studies in Trója, Prague. Sample was put into gelatine capsule and fastened by a drop of instant glue. Maximum field used was $\mu_0 H = 7$ T.

- Mössbauer spectroscopy was done on spectrometer Wissel using transmission arrangement and scintillating detector ND-220-M ($NaI:Tl^+$) at Joint Laboratory of Low Temperatures in Trója, Prague. α-Fe was used as a standard and fitting procedure was done using NORMOS program. Measurement at low temperature (4 K) under magnetic field 6 T was done in perpendicular arrangement.

- Optical measurements were done using 200 mW continuous wave 980 nm laser pointer (from Changchun New Industries Optoelectronics Tech. Co., Ltd., China) and spectra were observed using system composed of Olympus IX-71 microscope, spectroscope Acton SP2300 and CCD detector Princeton Instruments Spectra PRO400B cooled with liquid N_2 at Faculty of Mathematics and Physics, Charles University, Prague. Powder samples were placed between two 1 mm glass plates and illuminated by ca. 200 mW/cm^2 980 nm IR laser. Spectra were taken from the same side as illumination was done.

- Hydrodynamic diameter and ζ potential was measured on Malvern ZETASIZER NANO-ZS ZEN3600 at ICMM, CSIC, Madrid, using position 4.65 mm. Hydrophobic particles dispersed in hexane were mea-

sured in glass cell with 1 cm optical path (cobalt ferrite dipersion was diluted to such extent, that letters on the computer screen could be read through it without difficulty – such large concentration was neccesary due to small particle size and thus weak light scattering by them, otherwise scattering from dust would prevail at lower concentrations). Hydrophilic particles were measured in 0.01 M KNO_3 water dispersion, using plastic cell for size measurement or plastic zeta cell for zeta potential measurement.

- Thermogravimetric analysis was done on SEIKO model EXSTAR 6300 (simultaneous differential thermal analysis / thermogravimetric; range temperature: R. T. / 1000 °C) at ICMM, CSIC, Madrid; in air flow 100 ml/min and heating rate 10 °C/min to 900 °C. Amount of sample was 7-11 mg.

- Fourier transform infrared spectroscopy was done on Nicolet FT-IR 20SXC (4000-400 cm^{-1}) at ICMM, CSIC, Madrid. Samples were dried and incorporated into KBr tablet.

4.2 Chemicals

ethanol 96% v/v	Panreac, (USP, BP, Ph.Eur.)
2-propanol	Panreac, QP
1-pentanol	Aldrich, 99+%
n-hexane	Sigma-Aldrich, anhydrous 95%
dimethyl sulfoxide	Fluka, puriss. p.a. $\geq$ 99.5% (GC)
toluene	Merck, GR for analysis, ACS, ISO, Reag.Ph.Eur.
1-octadecene	Aldrich, technical grade. 90%
oleic acid	Aldrich, tech. 90%
oleylamine	Aldrich, tech. 90%
1,2-dodecanediol	Aldrich, 90%
ferric acetylacetonate	Fluka, purum $\geq$ 97.0% (RT)
cobalt(II) acetylacetonate	Aldrich, 97%
sodium hydroxide	Aldrich, ACS reagent, pellets 97+%
myristic acid	Fluka, purum $\geq$ 98.0% (GC)
iron(III) nitrate nonahydrate	Fluka, puriss. p.a.
cobalt(II) nitrate hexahydrate	Penta-chemicals, p.a.
meso-2,3-dimercaptosuccinic acid	Fluka, purum. $\geq$ 97% (T)

ammonium fluoride	Lach-Ner, p.a.
yttrium(III) nitrate hexahydrate	Aldrich, 99.8% trace metals basis
erbium(III) nitrate hexahydrate	Aldrich, 99.9% metals basis
ytterbium(III) nitrate pentahydrate	Aldrich, 99.9% metals basis
lanthanum(III) nitrate hexahydrate	Fluka, puriss. p.a.

4.3 General hydrothermal procedure

In a typical hydrothermal synthesis, the amount of chemicals used was: sodium hydroxide 6 mmol (240 mg), oleic acid 12 mmol (3.39 g), metal nitrate 1 mmol, ethanol 10 ml, water 20 ml.

1. The reagents were mixed in following order: NaOH, 2 ml of water, ethanol, oleic acid, water solution of metal salt and optionally other salt (e.g. ammonium fluoride to prepare fluorides). Final step was done with sonication and vigorous stirring.

2. Reaction mixture was put into teflon liner (volume 50 ml), enclosed in the autoclave Berghof DAB-2 and placed into oven for 10 to 16 hours.

3. After cooling of the autoclave, the final mixture consists of the following phases: upper oleic phase (in some cases with small amount of nanoparticles), aqueous phase and sedimented particles. The liquid phases were discarded. Remaining particles were dispersed in hexane.

4. Purification: particles dispersed in hexane (5 ml) were precipitated by ethanol (5 to 15 ml) and separated by centrifugation (4500 rpm for 5 minutes) or by magnet in case of magnetic particles. This was repeated 4 times. After each addition of ethanol or hexane, the mixture was briefly sonicated to speed up washing or particles redispersion.

5. Finally, the particles were redispersed into hexane (10 ml) and centrifuged (3000 rpm for 5 minutes) to remove bigger agglomerates.

4.4 Magnetic particles

For the synthesis of cobalt ferrite particles, 1 mmol of $Co(NO_3)_2$, 2 mmol $Fe(NO_3)_3$, and 10 mmol of NaOH was used. Several experiments were carried out with changed fatty acid (oleic/myristic acid), amount (10/20 ml) or

type (ethanol/1-pentanol) of alcohol (total amount of alcohol and water was always 30 ml) and reaction temperature (180/200 °C). The naming scheme is demonstrated on following example:
ole-eth/w-1/2-180: oleic acid 12 mmol, NaOH 10 mmol, $Fe(NO_3)_3$ 2 mmol, $Co(NO_3)_2$ 1 mmol, ethanol 10 ml, H_2O 20 ml (ethanol/water ratio is 1/2), 180 °C for 16 hours.

One sample was prepared using roughly triple amount of oleic acid and oleate (which, in case of Fe_3O_4, is reported to lead to 15 nm particles [7]):
ole3x-eth-1/2-180: NaOH 28 mmol (1.12 g), oleic acid 38 mmol (10.74 g), $Fe(NO_3)_3$ 2 mmol, $Co(NO_3)_2$ 1 mmol, ethanol 10 ml, water 20 ml

Two samples of cobalt ferrite particles were prepared by other methods inspired by organic decomposition:
acac-toluene-200: $Fe(acac)_3$ 2 mmol (0.706 g), $Co(acac)_2$ 1 mmol (0.257 g), 1,2-dodecanediol 10 mmol (2.023 g), oleic acid 6 mmol (1.70 g), oleylamine 6 mmol (1.60 g) and 20 ml of toluene were put into autoclave tube, stirred until dissolution, closed and heated to 200 °C for 16 hours.
ole-tol/w-4/1-200: NaOH 10 mmol (0.400 g), oleic acid 12 mmol (3.39 g), ethanol 10 ml, water 10 ml, $Fe(NO_3)_3$ 2 mmol (0.808 g), $Co(NO_3)_2$ 1 mmol (0.291 g) were mixed as in hydrothermal procedure. During stirring and sonication, black phase with metal oleates was formed. 10 ml of toluene was added to extract these oleates. After stirring and sonication, the water phase was discarded. Resulting toluene phase was put into autoclave tube together with 5 ml of water and 10 ml more of toluene and heated to 200 °C for 16 hours.

One sample was prepared by organic decomposition in octadecene:
ole-octdec-315: oleic acid 20 mmol, NaOH 16 mmol, $Fe(NO_3)_3$ 4 mmol, $Co(NO_3)_2$ 2 mmol, ethanol 5 ml, H_2O 10 ml were mixed as in hydrothermal procedure and 10 ml of hexane was added. Upper organic phase with Fe, Co oleates and 4 mmol of oleic acid was formed. Water phase was discarded and organic phase was washed with 10 ml of water. Hexane solution of oleates and oleic acid was mixed with 30 ml of octadecene, magnetically stirred and heated to 150 °C to evaporate hexane. Then, it was heated under reflux condenser and flow of N_2 to 200 °C and mantained at this temperature for 30 minutes. Then, it was heated to 315 °C at heating rate 5 °C / min and refluxed for 2 hours. After cooling, 30 ml of isopropanol was added, particles were magnetically separated and washed 2 times by redispersion in hexane and precipitation by acetone. Finally, they were redispersed into 15 ml of hexane.

4.5 Surface modification of $CoFe_2O_4$

For surface modification with 2,3-dimercaptosuccinic acid, procedure based on [8] was used (it was designed for magnetite particles prepared by organic decomposition).

Magnetic particles were precipitated by addition of ethanol to 2 ml of hexane dispersion (ca. 50 mg of particles by ICP-AES, not counting oleic surface layer). Solvents were removed using magnet, and a mixture of 25 ml of toluene and a solution of 90 mg of meso-1,2-dimercaptosuccinic acid (DMSA) in 5 ml of dimethyl sulfoxide was added. Reaction mixture was sonicated for 5 min and mechanically stirred 24 hours. During this time, modified particles precipitated. Solvent was discarded and particles were washed with mixture of 20 ml of ethanol and 20 ml of acetone followed by centrifugation at 9000 rpm for 5 min. Washing was repeated 3 times. Particles were redispersed in ca. 10 ml of water and 4 mg of NaOH was added. Dispersion was dialyzed in 4.5 l of deionized water for 72 hours. Final pH was around 6.

Same procedure was tried with lower DMSA/ferrite ratio (because DMSA is expensive), namely: 100 mg of particles, 25 ml toluene, 5 ml DMSO, 100 mg DMSA and, at final step, 8 mg NaOH. The modification was succesful, although more time for stirring was needed (30 hours).

4.6 Up-conversion particles

For the synthesis of $NaYF_4$ particles, following chemicals were used (after preparing oleic acid - oleate - water - ethanol solution as described in general procedure): solution of 0.83 mmol of $Y(NO_3)_3$, 0.15 mmol of $Yb(NO_3)_3$ and 0.02 mmol of $Er(NO_3)_3$ was prepared and added to oleate solution. Subsequently, solution of 4 mmol of NH_4F was added and the mixture was only briefly stirred and not sonicated (samples **Y-160**, **Y-180**, **Y-190**, **Y-200** – numbers indicate temperature of hydrothermal treatment during 10 hours). Similar procedure was repeated with 0.83 mmol of $La(NO_3)_3$, 0.15 mmol of $Yb(NO_3)_3$, 0.02 mmol of $Er(NO_3)_3$ and 3 mmol of NH_4F, with treatment for 10 hours at indicated temperature (samples **La-160**, **La-180**, **La-190**, **La-200**). After washing with hexane and ethanol, two phases were obtained: A – stable dispersion in hexane, B – precipitate obtained after final centrifugation (usually showing strong up-conversion).

When the reaction mixture is well stirred and sonicated, obtained par-

ticles in sediment (B) show much weaker up-conversion in case of $NaYF_4$, and no up-conversion at all for LaF_3 (tried for 170 and 200 °C). Samples obtained at 170 °C from sonicated reaction mixtures are labeled **Y-170-son** and **La-170-son**. Sample Y-170-son-A (hexane dispersion) shows weak red up-conversion visible in dark (not observed for previous samples in hexane dispersion).

Up-conversion particles were obtained also using EDTA instead of oleic acid. Following chemicals were mixed in order: 1.66 mmol of $Y(NO_3)_3$, 0.3 mmol of $Yb(NO_3)_3$, 0.04 mmol of $Er(NO_3)_3$ in 10 mmol of water, 20 ml of ethanol, 2 mmol of EDTA (disodium salt dihydrate), 4 mmol of oleylamine and 8 mmol NH_4F in 2 ml of water. Nearly clear solution was obtained, which was subsequently put into autoclave and treated 24 hours at 200 °C. After cooling, the clear water solution was discarded and remaining particles were dispersed in 10 ml of ethanol, 5 ml of hexane was added, and particles were separated by centrifugation at 4500 rpm for 5 minutes. This washing step was repeated 4 times. Particles were dried at 25 °C. Yield was 304 mg (sample **Y-EDTA-4F-200**). Same procedure was repeated with 16 mmol of NH_4F (sample **Y-EDTA-8F-200**, yield 377.6 mg). Obtained particles could be dispersed in water and obtained dispersion was stable for several hours.

Chapter 5

Results and discussion

5.1 Magnetic particles: size and composition

Size and composition of magnetic particles were obtained by:

- atomic emission spectroscopy, measuring ratio Fe/Co of as-prepared samples and samples after modification with 1,2-dimercaptosuccinic acid (table 5.1)
- manual measurement of TEM photographs, from which estimate of size distibution, average size and standard deviation was obtained (weighted by number and volume, i.e. size^3); also number of measured particles is given (size was measured in two perpendicular directions and geometrical mean was calculated; table 5.2, figures 5.1, 5.2, 5.3, 5.4, 5.5)
- dynamic light scattering (DLS) measurement to obtain Z-average size, polydispersity index of cumulants mean, peak of intensity distribution; also counts per second and attenuator is given (table 5.2)
- powder X-ray diffraction; profile analysis was done by WinPLOTR (figure 5.6)

Table 5.1: Fe/Co ratio for hydrophobic (as-prepared) and hydrophilic (modified with DMSA) particles measured by atomic emission spectroscopy

sample	as-prepared	with DMSA
ole-eth/w-1/2-180	2.89	2.20
ole-pen/w-1/2-180	1.96	2.17
myr-eth/w-1/2-180	2.03	2.19
ole-eth/w-2/1-180	2.14	2.31
ole-eth/w-1/2-200	2.69	2.87
ole-pen/w-1/2-200	1.94	2.09
myr-pen/w-1/2-200	1.91	2.03
ole3x-eth/w-1/2-180	2.38	2.59
acac-toluene-200	2.07	2.38
ole-tol/w-4/1-200	2.00	2.14
ole-octdec-315	2.67	

Table 5.2: Size of hydrophobic (as-prepared) particles measured by TEM (weighted by number and volume: size^3; number of particles measured) and dynamic light scattering (Z-average size, polydispersity index, peak of distribution and its contribution to whole distribution)

sample	TEM size [nm]			DLS				
	by number	by volume	# p.	size	PDI	peak	kcps	attn
ole-eth/w-1/2-180	7.4 ± 1.8	8.7 ± 2.2	203	9.1 nm	0.28	7.9 nm (83%)	202	10
ole-pen/w-1/2-180	5.8 ± 1.1	6.4 ± 1.2	301	5.3 nm	0.12	5.4 nm (94%)	163	11
myr-eth/w-1/2-180	7.2 ± 1.9	8.6 ± 2.3	279	8.8 nm	0.23	9.5 nm (88%)	160	11
ole-eth/w-2/1-180	6.0 ± 1.9	8.3 ± 3.02	205	6.9 nm	0.21	6.6 nm (94%)	198	11
ole-eth/w-1/2-200	7.1 ± 2.4	11.0 ± 4.6	229	9.2 nm	0.24	9.4 nm (90%)	213	10
ole-pen/w-1/2-200	6.1 ± 1.2	6.8 ± 1.4	432	6.2 nm	0.20	5.8 nm (94%)	186	11
myr-pen/w-1/2-200	5.7 ± 1.1	6.4 ± 1.4	219	5.6 nm	0.16	6.3 nm (99%)	167	11
ole3x-eth/w-1/2-180	6.0 ± 1.3	6.8 ± 1.5	150	6.6 nm	0.20	6.4 nm (96%)	166	11
acac-toluene-200	7.8 ± 1.6	8.8 ± 1.8	116	10.0 nm	0.17	11.5 nm (98%)	163	10
ole-tol/w-4/1-200	6.2 ± 1.2	6.9 ± 1.4	718	6.0 nm	0.09	6.2 nm (100%)	201	11
ole-octdec-315	8.2 ± 1.0	8.5 ± 1.1	100	37.8 nm	0.21	50.4 nm (100%)	195	7

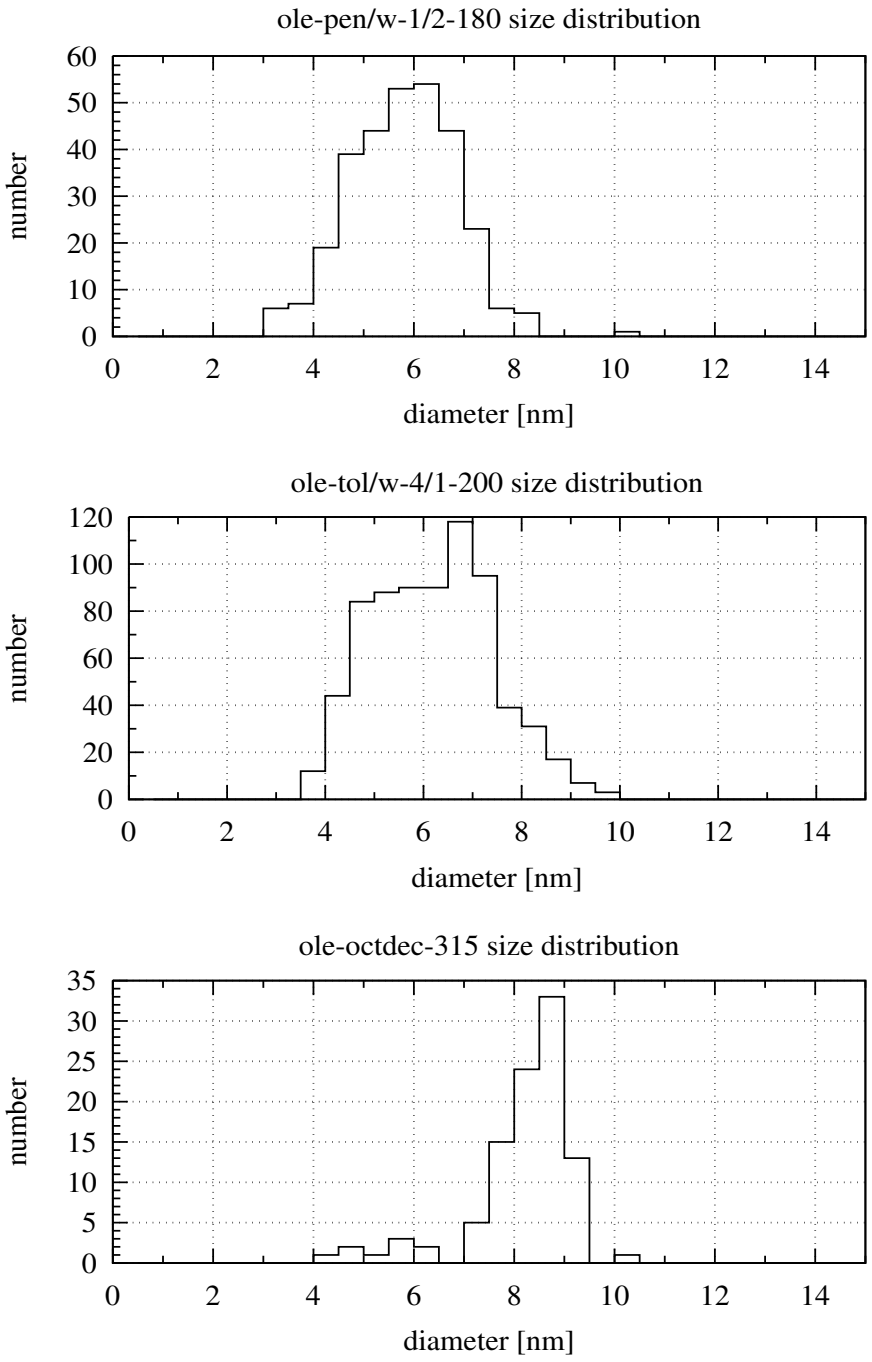

Figure 5.1: Size histograms from measurement of TEM photographs of samples **ole-pen/w-1/2-180**, **ole-tol/w-4/1-200**, **ole-octdec-315** (best samples of hydrophobic $CoFe_2O_4$ from each method)

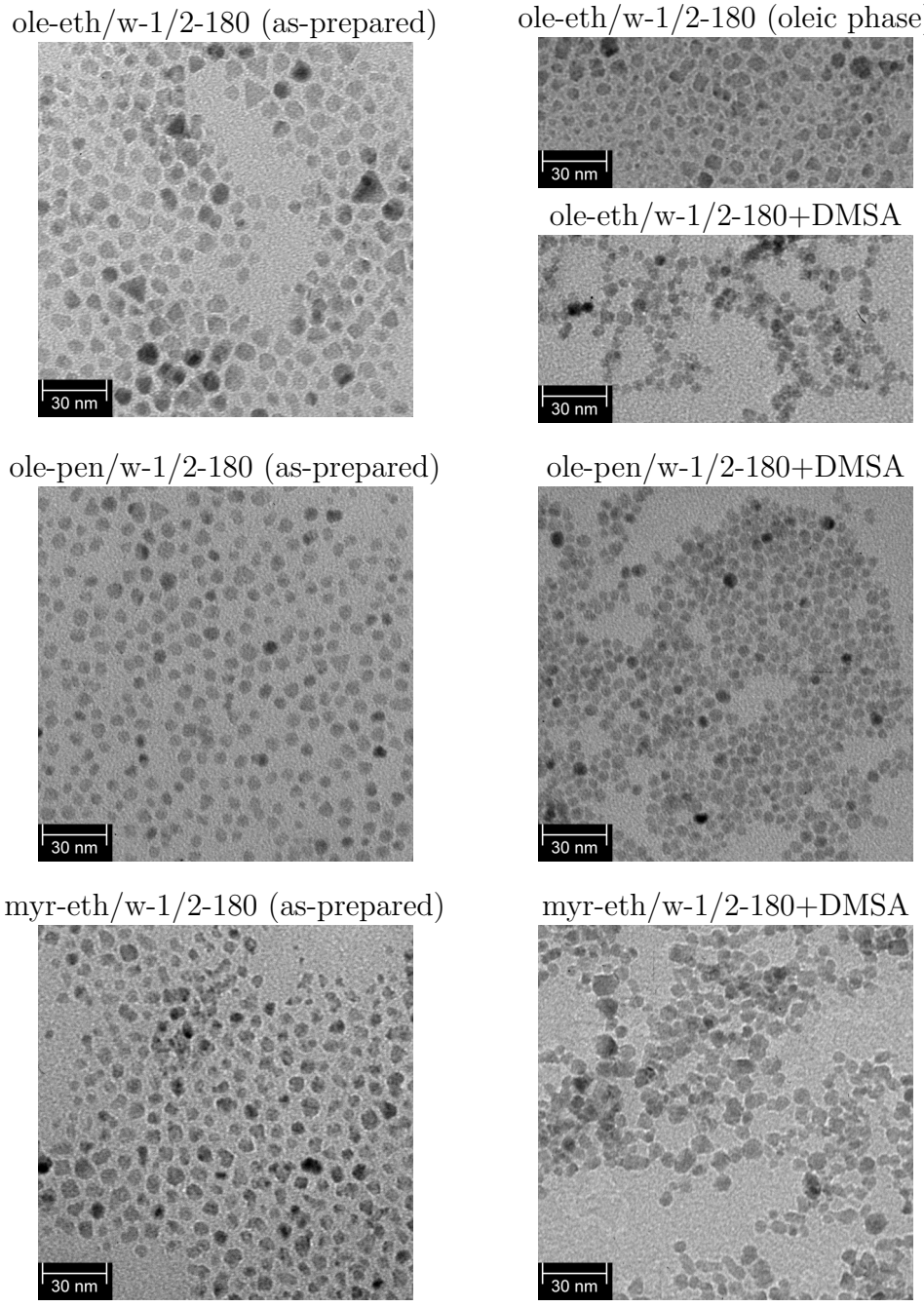

Figure 5.2: TEM pictures of hydrothermally prepared $CoFe_2O_4$ particles: **ole-eth/w-1/2-180**, **ole-pen/w-1/2-180**, **myr-eth/w-1/2-180** – as-prepared (hydrophobic) and modified with DMSA (hydrophilic). For the first sample, also particles obtained from oleic phase after hydrothermal treatment are shown.

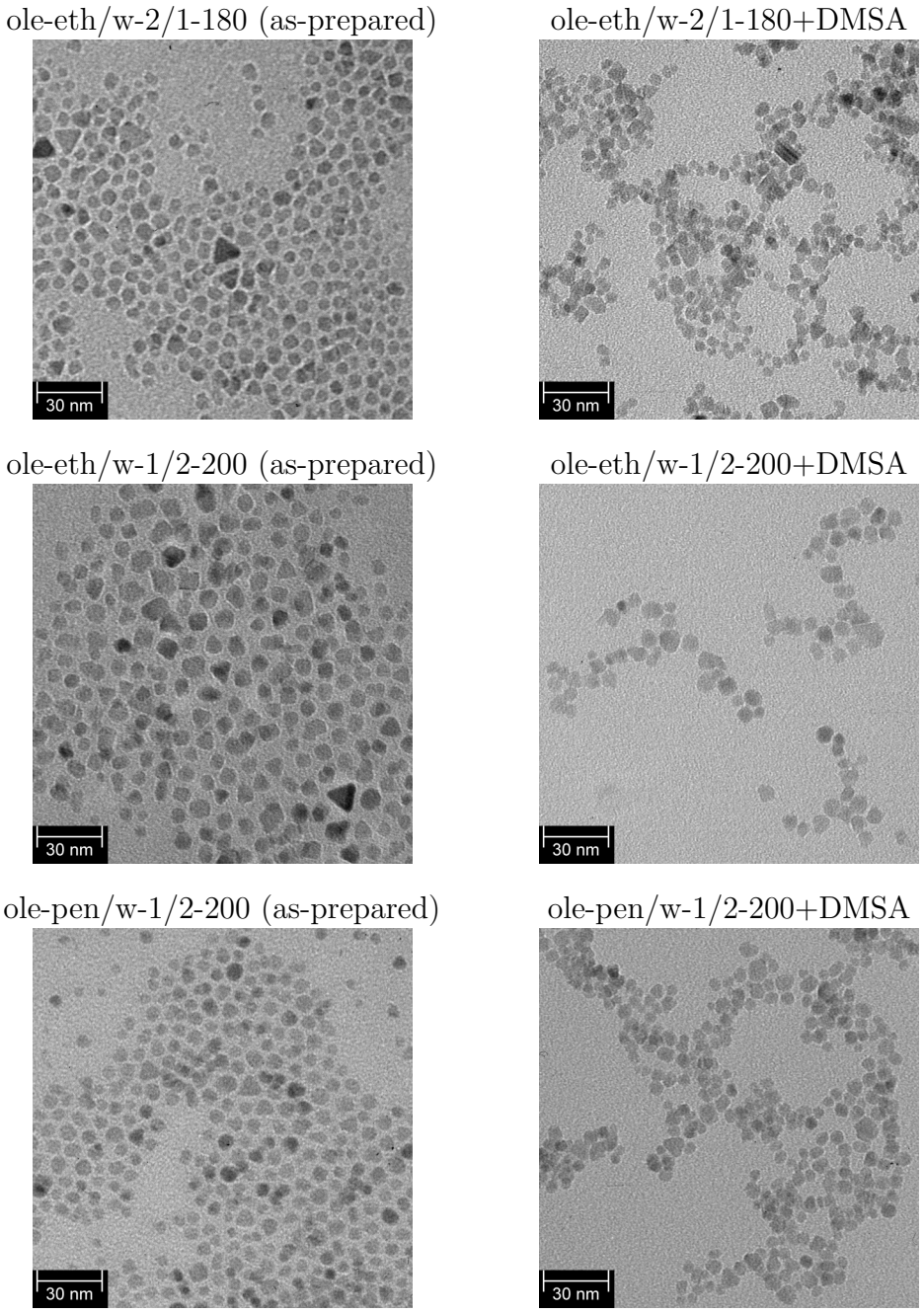

Figure 5.3: TEM pictures of hydrothermally prepared $CoFe_2O_4$ particles: **ole-eth/w-2/1-180**, **ole-eth/w-1/2-200**, **ole-pen/w-1/2-200** as-prepared (hydrophobic) and modified with DMSA (hydrophilic).

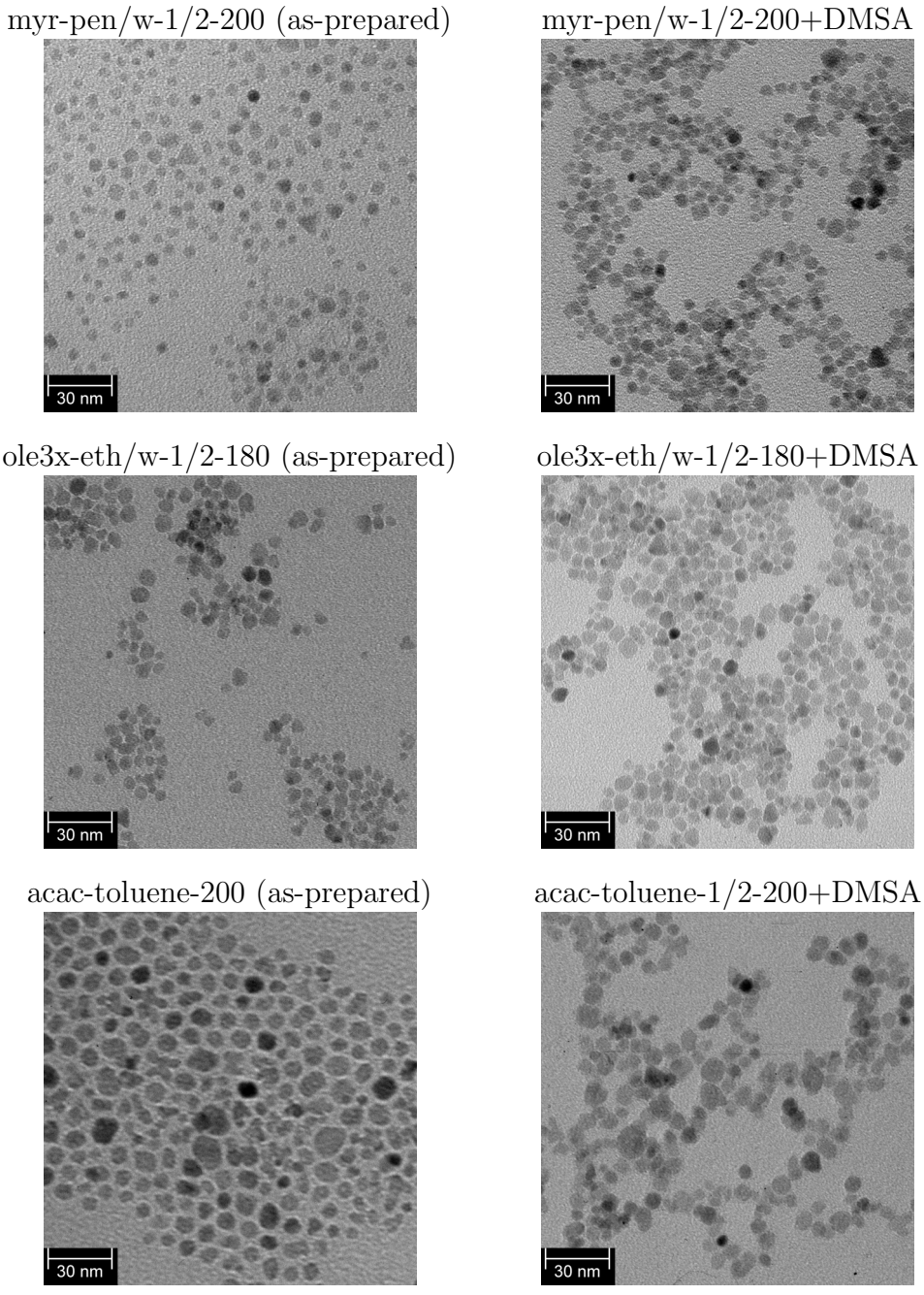

Figure 5.4: TEM pictures of hydrothermally prepared $CoFe_2O_4$ particles: **myr-pen/w-1/2-200**, **ole3x-eth/w-1/2-180**; and by solvothermal organic decomposition: **acac-toluene-200** – as-prepared (hydrophobic) and modified with DMSA (hydrophilic).

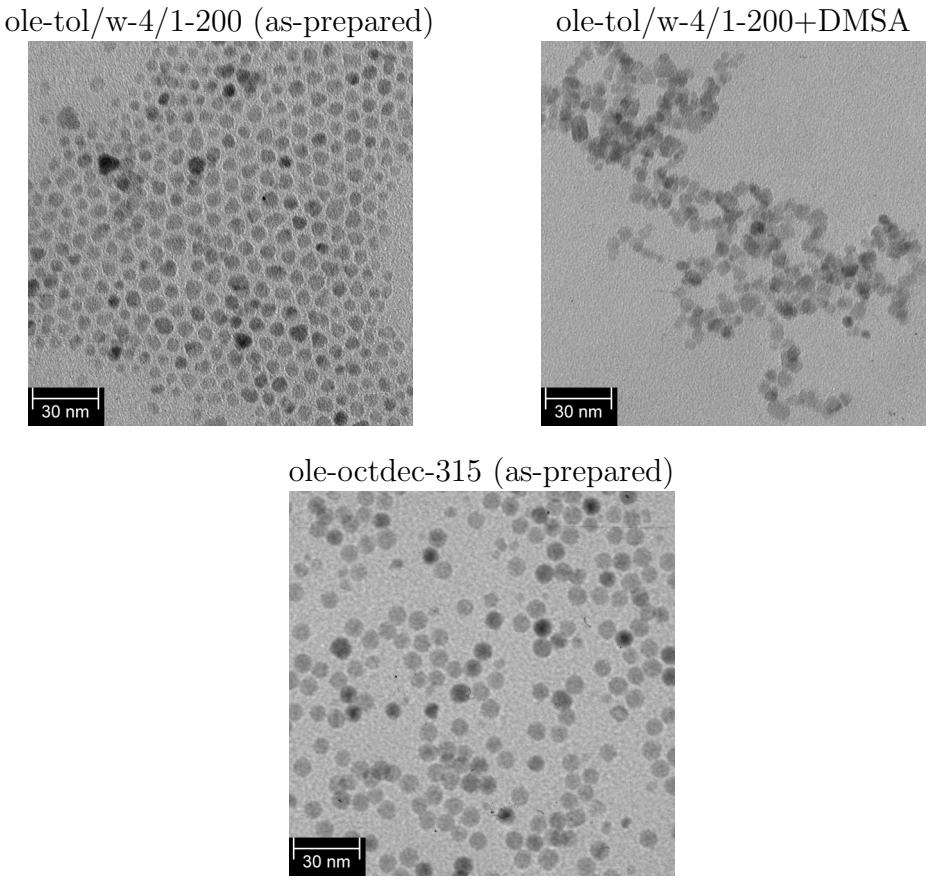

Figure 5.5: TEM pictures of sample **ole-tol/w-4/1-200**, prepared from oleates in toluene under pressure, and **ole-octdec-315**, prepared by organic decomposition of oleates in octadecene.

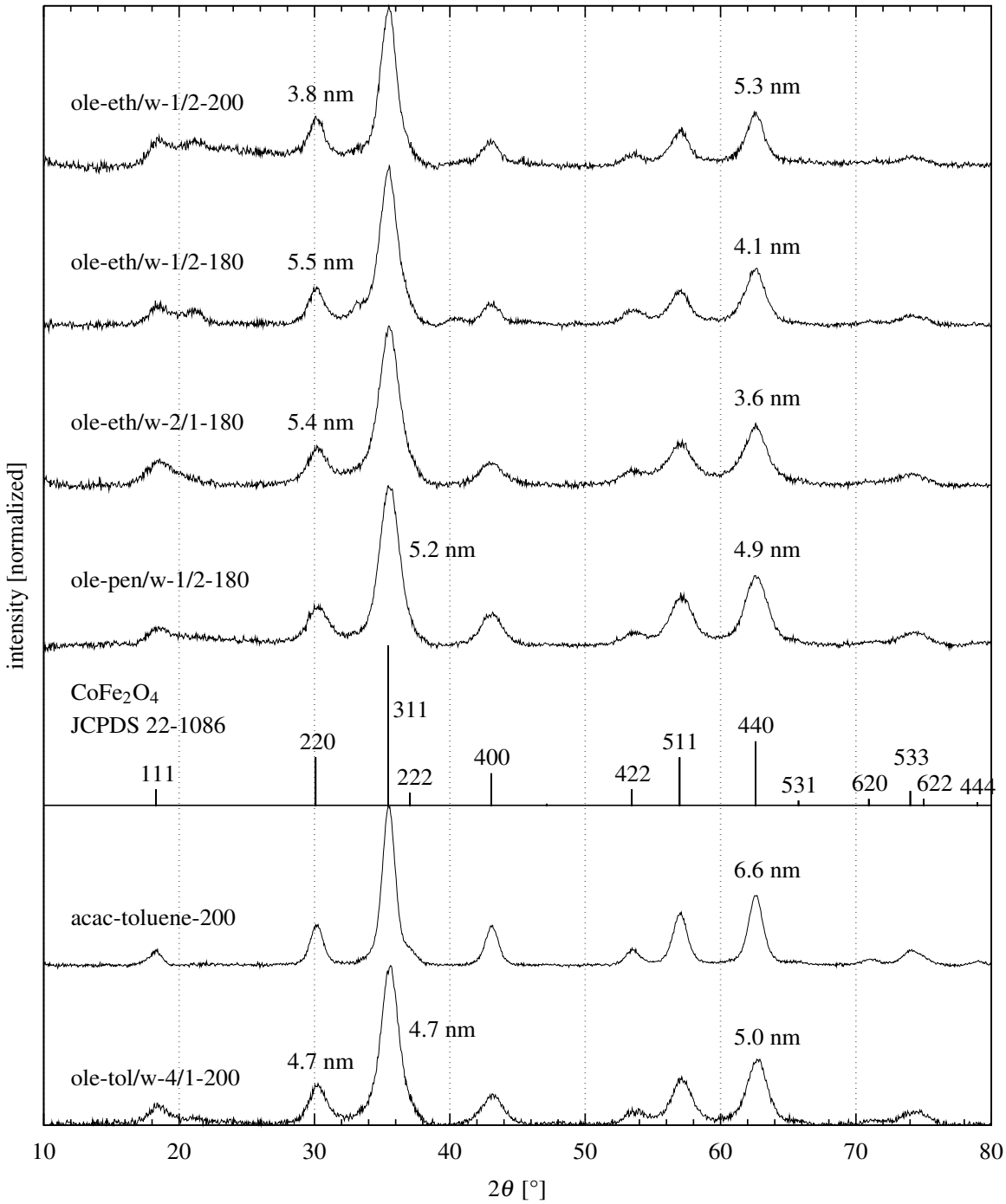

Figure 5.6: Powder X-ray diffraction of $CoFe_2O_4$ particles with sizes obtained from profile analysis. Note that XRD gives lower bound of particle size distribution.

5.2 Discussion of hydrothermal synthesis

5.2.1 Oleic acid – sodium oleate system

For hydrothermal synthesis, oleic acid and sodium oleate, as capping agents for nanoparticles, should be dissolved in some solvent, which could also dissolve other reactants. Because sodium oleate has small solubility in pure water, mixture of water and ethanol was used. Sodium oleate was prepared directly from oleic acid and sodium hydroxide.

$$C_{18}H_{33}COOH + NaOH \rightarrow C_{18}H_{33}COONa + H_2O$$

Water solution of NaOH cannot be used to react directly with oleic acid because insoluble oleate is immediately formed. As NaOH is difficult to dissolve in ethanol, it was first dissolved in small amount of water and then ethanol was added. This solution can be mixed directly with oleic acid to form clear solution. It was found that if too little water is used, oleate precipitate, because it is not well soluble in pure ethanol. Minimum amount of water was found to be 1 ml for 0.4 g (10 mmol) of NaOH.

5.2.2 Metal oleate formation

After adding solution of iron and cobalt nitrate which serves as precursor, reaction mixture becomes turbid, and after sonication two phases are formed: water phase (colorless, but not entirely clear) and organic phase containing metal oleates and remaining oleic acid. Ethanol and sodium oleate are distributed between these two phases.

$$3\,C_{18}H_{33}COONa + Fe(NO_3)_3 \rightarrow Fe(C_{18}H_{33}COO)_3 + 3\,NaNO_3$$
$$2\,C_{18}H_{33}COONa + Co(NO_3)_3 \rightarrow Co(C_{18}H_{33}COO)_2 + 2\,NaNO_3$$

The composition of reaction mixture before hydrothermal treatment is following:

$Fe(C_{18}H_{33}COO)_3$	2 mmol
$Co(C_{18}H_{33}COO)_2$	1 mmol
$C_{18}H_{33}COOH$	2 mmol
$C_{18}H_{33}COONa$	2 mmol
$NaNO_3$	8 mmol
water + ethanol	30 ml

This observation of two liquid phases contradicts with the proposal of authors of hydrothermal synthesis in fatty acid - ethanol - water system [2, 7]. They propose liquid-solid-solution (LSS) system in which solid phase (sodium oleate or linoleate) acts as a medium for exchange of metal ions and particle formation. Although using such large amount of oleic acid and sodium oleate (sample ole3x-eth/w-1/2-180) actually leads to precipitation of sodium oleate, this phase doesn't seem to be critical for nanoparticle synthesis.

5.2.3 Formation of particles

During the hydrothermal treatment, metal oleates are hydrolyzed and particles of $CoFe_2O_4$ capped with oleic acid anions are formed. The process is illustrated on figure 5.7.

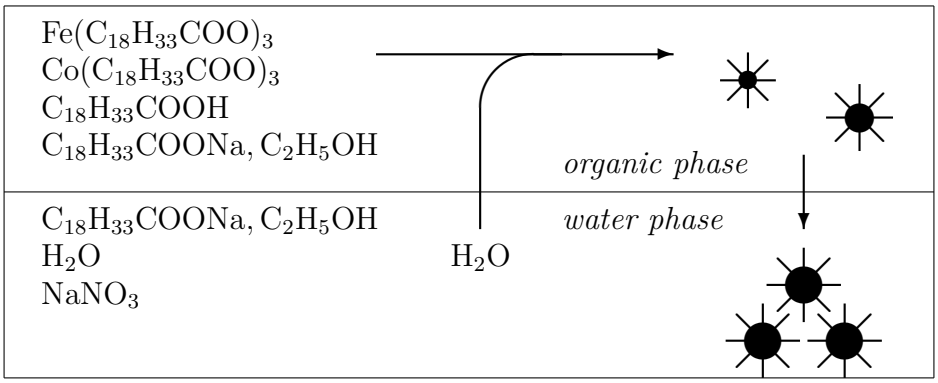

Figure 5.7: Schematic depiction of hydrothermal formation of nanopaticles: metal oleates are hydrolyzed, and formed nanoparticles precipitate into water phase after reaching critical diameter

From the dependence of particle parameters on reaction conditions, following conclusions can be made:

- Particle size and distribution are only weakly dependent on choice of fatty acid (oleic/myristic), although in case of myristic acid, particles were smaller by 0.2 to 0.4 nm.

- No clear dependence of particle size on temperature (180/200 °C) was found. Results suggest that size distribution is worse for higher tem-

perature. In case of organic decomposition method, it is observed that higher temperature leads to bigger particles [1, 8].

- The major part of ethanol is present in water phase, but in case of pentanol, it is the opposite (observation of phase volumes).
- Higher content of alcohol in organic phase leads to better size distribution and smaller particles.
- In case of ethanol, oleic phase contains some particles after reaction (figure 5.2, upper right), but their size distribution is very bad. This is not the case of pentanol where no particles are observed in organic phase. Alcohol content in organic phase thus plays some role in particle precipitation from organic phase during hydrothermal treatment.
- Higher ethanol/water ratio leads to smaller particles, but dependence is not as strong as reported in [7] for magnetite (16 vs. 6 nm). However, ethanol is not good reaction medium for the reason of bad size distribution.
- Particles modified with dimercaptosuccinic acid seemed to be a little smaller and their Fe/Co ratio was higher in almost all cases. This suggest that during surface modification, thin surface layer with higher Co content is dissolved. Rate of decomposition for iron oleate in hydrothermal conditions could be higher than for cobalt oleate, but finally all oleates are decomposed. Observed Fe/Co ratio could be explained also by presence of particles with high Co content which are completely dissolved during surface modification. But the difference in Fe/Co ratio is not very high, especially in case of particles with good size distribution, so effect of different rates of oleates decomposition plays only minor role.

From these facts, it could be concluded that nucleation and growth of particles takes place continually (no temperature dependence of size) and size of particles is controlled by precipitation from organic phase (dependence on alcohol type and content). After reaching certain size, particles are not more stable in organic phase, and they precipitate into water phase where their growth is suppressed.

It is reported [1, 6] that for organic decomposition method, separation and control of nucleation and growth phase is critical for good size distribution. Also temperature dependence is more pronounced [1, 8]. This shows

that mechanism involved in particle formation is different in hydrothermal and organic decomposition method. Especially in the case of decomposition of oleate presursors in octadecene, it is not clear how oleate is transformed into oxide (only clear route would be formation of oleic acid anhydride). The overall process could be termed as pyrolysis with production of various undefined organic compounds. However, in the case of acetylacetonate precursors and in the presence of 1,2-dodecanediol, also milder decomposition routes could be proposed (sample acac-toluene-200 and [1]).

Organic decomposition of acetylacetonate precursors can take place also at lower temperatures as was shown for sample acac-toluene-200 (solvothermal reaction in toluene at 200 °C) but the size distribution of preparted particles is not as good as in case of well controlled process with nucleation period at the beginning of reaction, where diphenylether (b.p. 265 °C) or dibenzylether (b.p. ≈300 °C) are used as solvents.

One sample (ole-tol/w-4/1-200) was prepared by decomposition of iron and cobalt oleates in toluene under pressure in presence of water (to enable formation of oxides from oleates as the temperature is supposedly not high enough for pyrolysis). The size distribution obtained from TEM (figure 5.5, up) and especially from dynamic light scattering (table 5.2) is encouraging and this method warrants further study. The mechanism could be similar as in the case of hydrothermal method, but particles are not sedimented from organic phase after hydrothermal treatment and addition of ethanol is necessary.

5.3 Magnetic particles: surface characterization

Surface of magnetic particles was characterized by following methods:

- thermogravimetric analysis, to obtain percentage of organic material on the surface of particles (figures 5.8, 5.9, 5.10)
- infrared spectroscopy, to obtain type of molecules bonded to surface of particles (figure 5.11)
- hydrodynamic size and zeta potential was measured on dispersions of surface modified particles in 0.01 M KNO_3. pH was adjusted by 0.01 M KOH, 0.01 M and 0.1 M HNO_3 (figure 5.12)

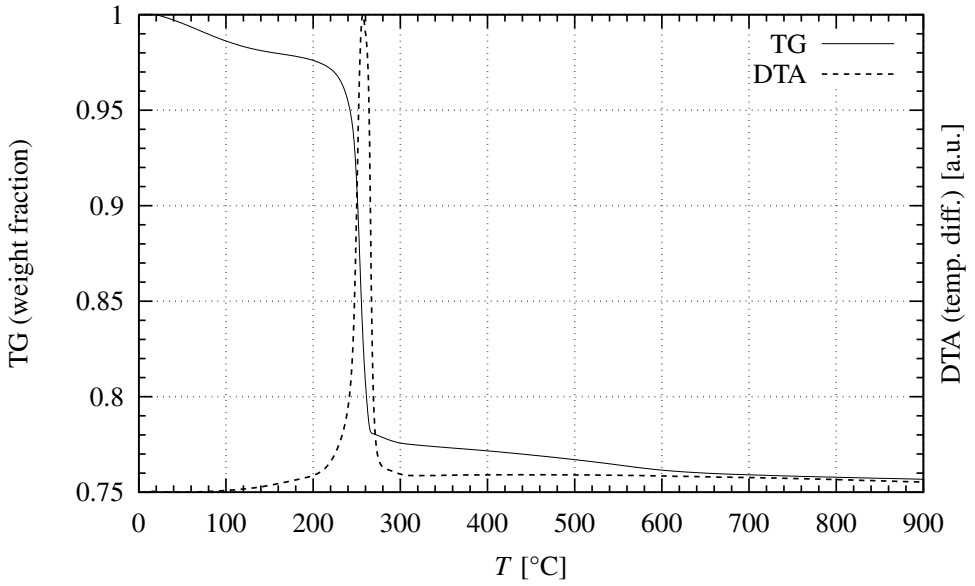

Figure 5.8: Thermogravimetric analysis of sample **ole-pent/w-1/2-200** (as-prepared, capped with oleic acid, hydrophobic)

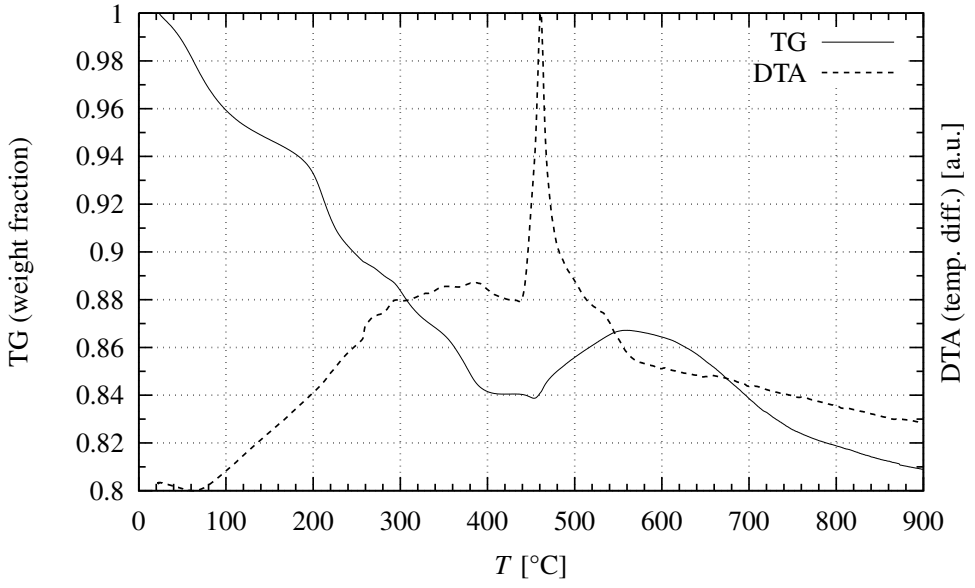

Figure 5.9: Thermogravimetric analysis of sample **ole-pent/w-1/2-200** (modified with dimercaptosuccinic acid, hydrophilic)

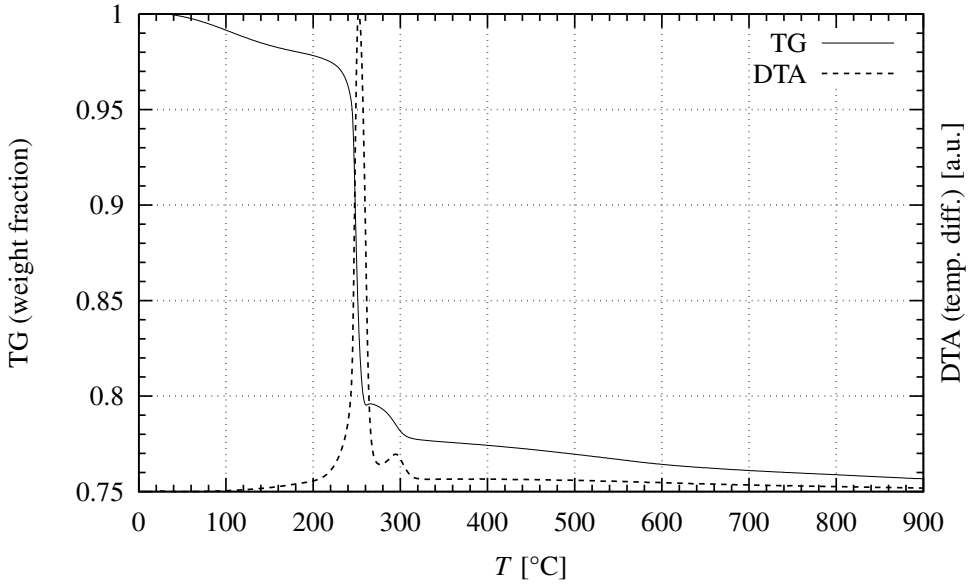

Figure 5.10: Thermogravimetric analysis of sample **ole-tol/w-4/1-200** (as-prepared, capped with oleic acid, hydrophobic)

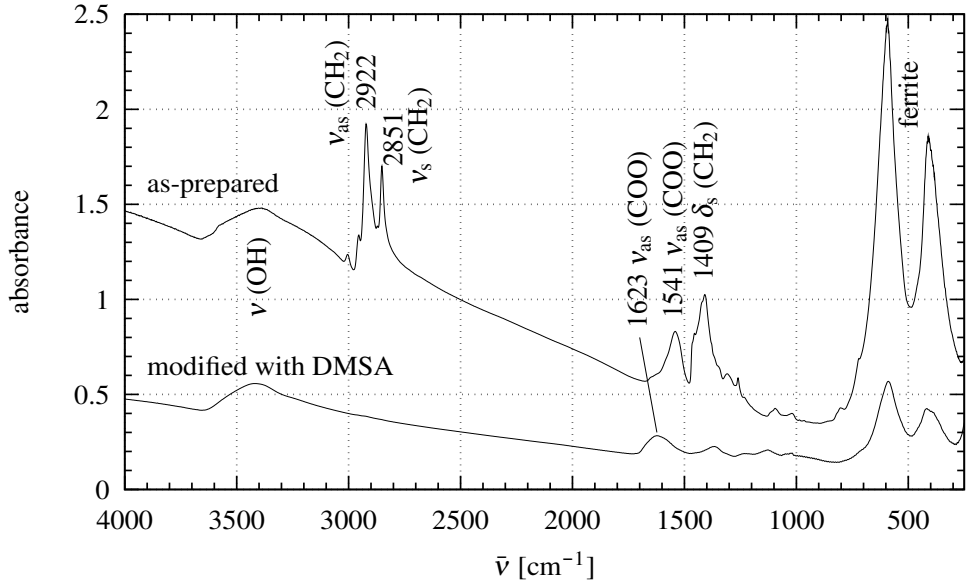

Figure 5.11: Infrared absorption spectra of sample **ole-pent/w-1/2-180**: as-prepared (capped with oleic acid, hydrophobic), modified with dimercaptosuccinic acid (hydrophilic). Assigned according to [47].

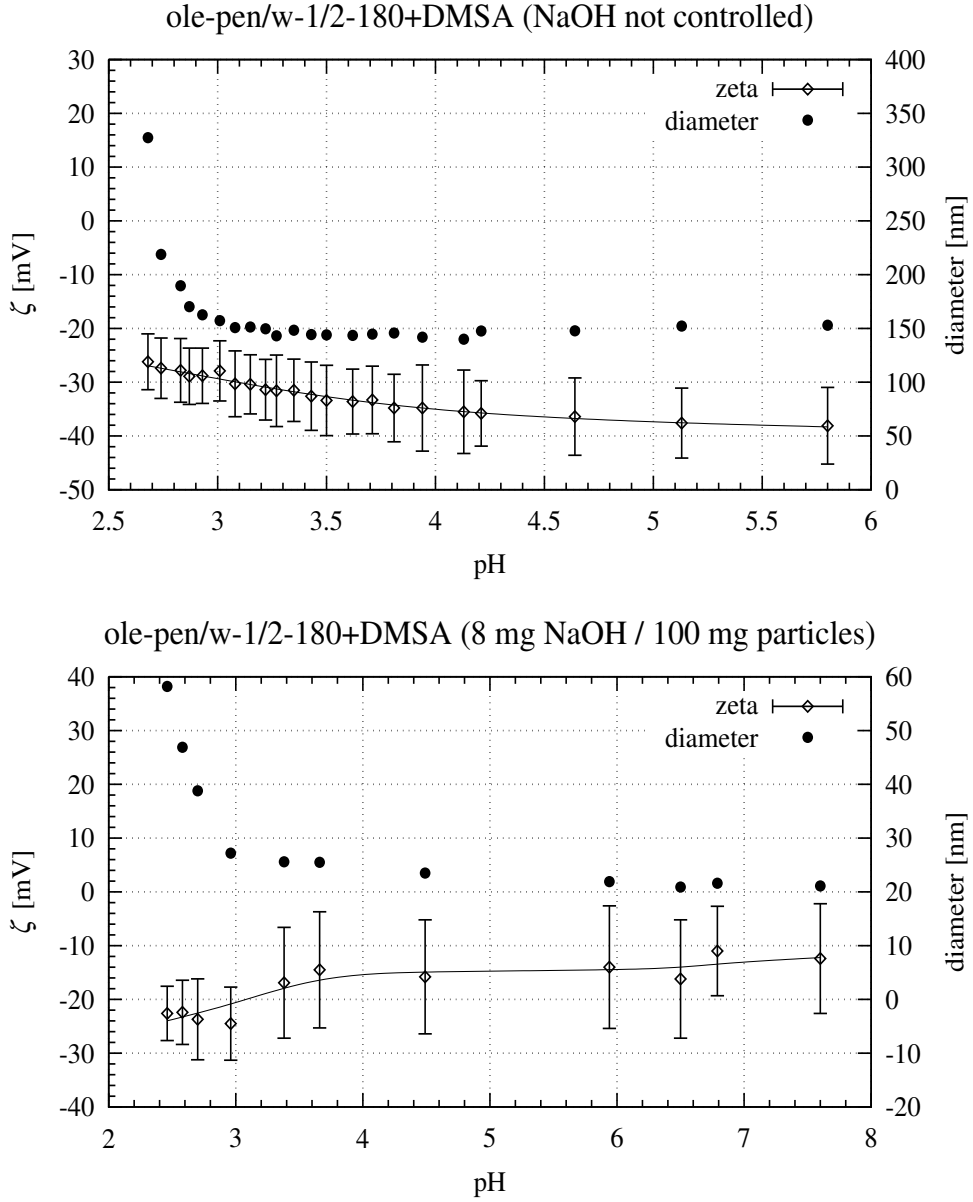

Figure 5.12: Zeta potential and hydrodynamic size measurement of water-dispersed particles of $CoFe_2O_4$ prepared in oleic acid - pentanol - water at 180 °C and modified by dimercaptosuccinic acid.

Hydrophobic particles prepared by hydrothermal method are covered with oleic acid, so only 75% of their mass is cobalt ferrite core (in case of 6 nm particles, figures 5.8, 5.10). Remaining mass can be attributed to oleic anions strongly bound to surface, as there is no peak for COOH group in IR spectrum at figure 5.11 (which would be at 1760-1700 cm^{-1} [47], table 7.23). About 3% could be attributed to hexane which evaporates slowly until rapid burning of whole organic layer occurs at around 250 °C. When particles are prepared in toluene, toluene is probably not fully removed by washing (excess peak in DTA at figure 5.10 at 290 °C in comparison with 5.8).

Surface of hydrophilic particles is different from previous case. Surface layer is thinner and forms only 20% of weight. There are no CH_2 groups, only COO groups of different origin (figure 5.11). During the heating, decomposition and evaporation takes place gradually, until sudden burning of sulfur occurs at 460 °C connected with increase of weight (sulfates are created). However at even higher temperatures, sulfur evaporates in form of SO_3, considering similar behaviour of $Fe_2(SO_4)_3$ (figure 5.9).

Zeta potential was negative down to pH 2.5, but for well dispersed particles of 20 nm hydrodynamic size, its value was not as negative as expected for stable dispersion. Possible reason could be non-adequacy of Smoluchowski approximation used in Zetasizer equipment for such small particles in water, or it just showed real zeta potential, which numerical value -15 mV could be appropriate for particles of such size.

5.4 Discussion of surface modification

One of the most usual methods of surface modification to make particles hydrophobic is coating with silica (SiO_2) created by hydrolysis of tetraethoxysilane. However, thickness of silica layer is not well controllable and particles tend to aglomerate (probably due to formation of Si–O–Si bonds between individual particles) and sediment after few weeks (observed in previous experiments not listed here).

Therefore, other type of modification was chosen, namely substitution of oleic acid ligands by 2,3-dimercaptosuccinic acid (DMSA). DMSA bonds to the particle through COO groups and SH groups are intended for further modifications for use in biomedical applications. This method was succesfully applied to the particles prepared by organic decomposition [8]. Modification takes place in mixture of toluene and dimethylsulfoxide, which well dissolves

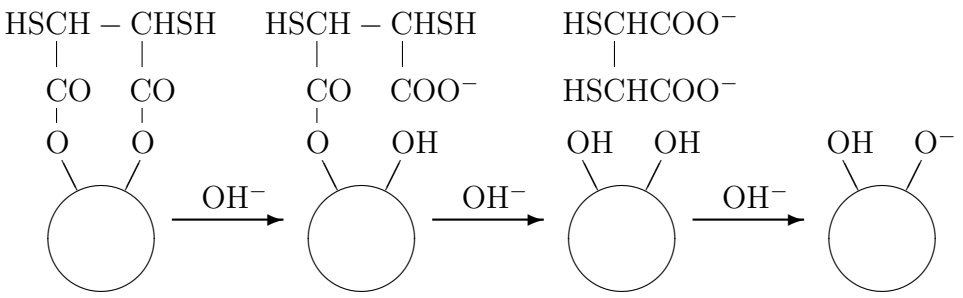

Figure 5.13: Scheme of NaOH function during redispersion in water after surface modification of magnetic particles with DMSA (clear water dispersion is produced only in the second case)

DMSA, and also hydrophobic particles can be well dispersed in it. However, modified particles are not more dispersible, and sediment on the walls of reaction wessel. After washing with ethanol and acetone, they are redispersed into water, but to obtain stable and clear dispersion, it is necessary to add some NaOH as was found by Roca [8]. Supposed scheme of NaOH function is depicted on figure 5.13 (Roca proposed only the first step).

However, as can be seen from previous scheme, adding more NaOH than neccesary leads to extraction of DMSA from particle surface and irreversible agglomeration of particles. It was observed, that only with well controlled amount of NaOH (in my case about 4 mg per 50 mg of particles, as 2 mg weren't sufficient for clearing of the dispersion), it was possible to obtain DLS size less than 100 nm, even without filtration through millipore filter. Difference can be seen also on TEM pictures: only samples ole-pen/w-1/2-180 and ole3x-eth/w-1/2-180 were prepared with controlled amount of NaOH, all other samples were prepared with approximately two drops of concentrated NaOH solution, i.e. not well defined amount. Also in [8], the amount of NaOH is not defined.

Further increasing of the amount of NaOH leads to precipitation of the particles. Increasing amount of NaOH even more leads again to dispersible particles, but dispersion is not clear (high agglomeration).

In this explanation, bonding to surface was considered only by COO^- groups, but coordination by SH cannot be ruled out (no ν(SH) at 2600 cm^{-1} was found). Further experiments with succinic, malic or tartaric acid could clear this issue.

5.5 Magnetic measurements

Magnetic properties of $CoFe_2O_4$ particles were investigated by SQUID magnetometry and Mössbauer spectroscopy of ^{57}Fe.

Particles were superparamagnetic and measurement of zero field cooling and field cooling curves (ZFC/FC) was done to obtain blocking temperature (figures 5.14, 5.16, table 5.3). Saturation of FC curve confirmed dipolar interactions between particles. Moreover, in case of hydrophilic particles with thin surface layer, where T_{B2} reaches 400 K, collective behaviour (creation of magnetic clusters) can be expected.

Superparamagnetic behaviour at 300 K was further confirmed by the measurement of hysteresis loop, which showed zero coercivity for all samples. From the hysteresis loop at 300 K, coercitive field H_c, remanent magnetization M_r and saturation magnetization M_s were obtained (table 5.3). Magnetization was calculated from its mass weighted form (as plotted in figures 5.15, 5.17) by multiplication with $CoFe_2O_4$ density $\varrho = 5300$ kg.m^{-3} (oleic surface layer was not subtracted).

Measured saturation magnetization at 10 K, $M_s = 68$ A.m^2.kg^{-1} is very good, compared to literature data on 5 nm $CoFe_2O_4$ particles, prepared by coprecipitation and heat-treated at 325 °C: $M_s = 13$ A.m^2.kg^{-1} at 5 T and 5 K, and it is closer to the value of bulk sample, $M_s = 93.9$ A.m^2.kg^{-1} [48]. However, the coercivity was found lower than reported value: $\mu_0 H_c = 1.45$ T. Differences in table 5.3 can be explained by wide size distribution of the samples prepared in ethanol – smaller particles have lower M_s and higher content of oleic acid on their surface.

Table 5.3: Magnetic properties of $CoFe_2O_4$ nanoparticles obtained from ZFC/FC measurement at 5 mT – blocking temperatures: T_{B1} (peak of ZFC), T_{B2} (intersection of ZFC and FC), parameters of hysteresis loop at 10 K: coercitive field, remanent magnetization and saturation magnetization at 7 T (saturation was not reached, see figures 5.15, 5.17)

sample	T_{B1}	T_{B2}	$\mu_0 H_c$	$\mu_0 M_r$	M_s [A.m^2.kg^{-1}]	$\mu_0 M_s$
ole-eth/w-1/2-180	222 K	318 K	1.14 T	0.181 T	45.1	0.30 T
ole-eth/w-2/1-180	226 K	362 K		0.112 T	28.2	0.19 T
ole-eth/w-1/2-200	268 K	380 K	1.12 T	0.238 T	57.1	0.38 T
ole-pen/w-1/2-180	191 K	286 K	1.16 T	0.267 T	67.7	0.45 T
ole-pen/w-1/2-180+DMSA	199 K	400 K	0.94 T	0.248 T	67.6	0.45 T
ole-tol/w-4/1-200	274 K	397 K	1.26 T	0.275 T	67.1	0.45 T

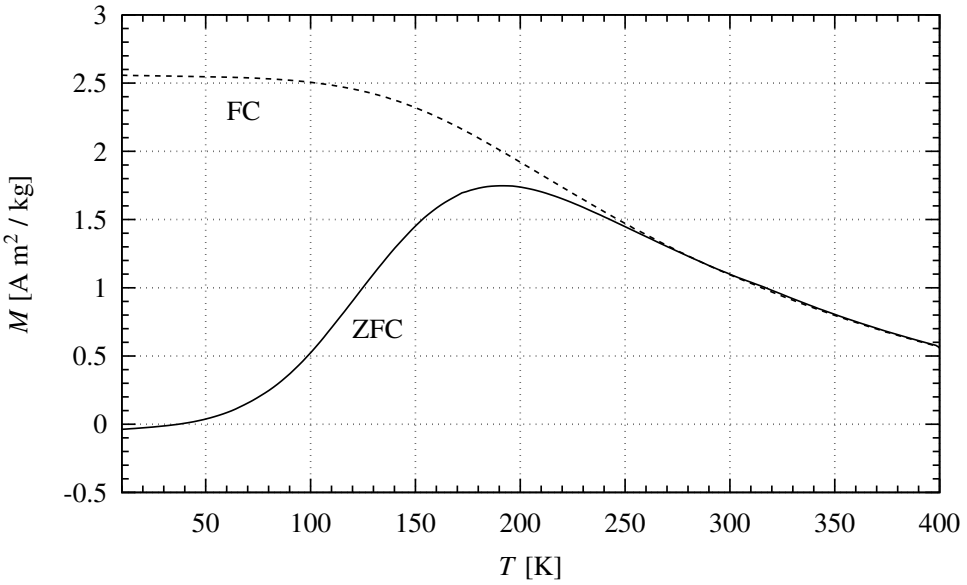

Figure 5.14: ZFC-FC measurement of sample **ole-pen/w-1/2-180** at 5 mT.

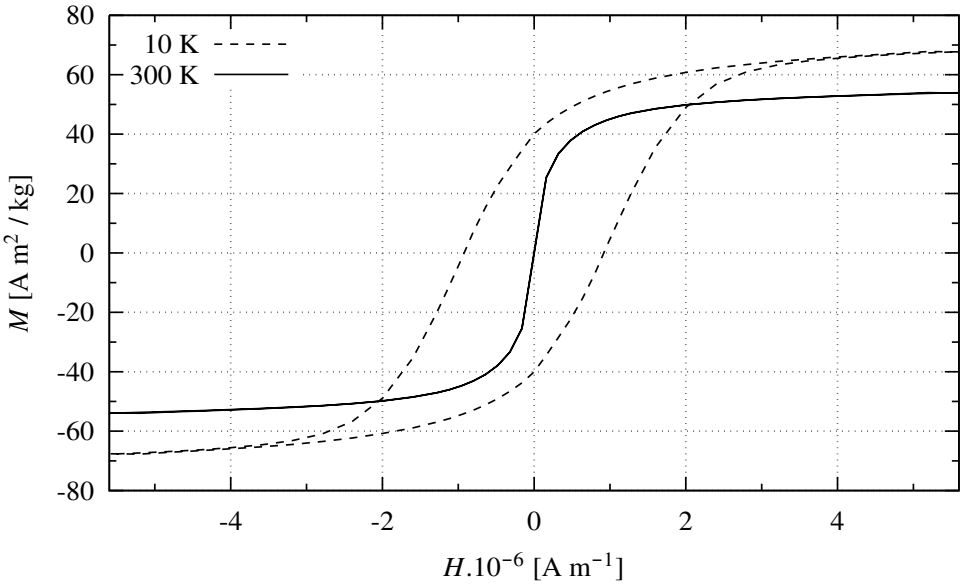

Figure 5.15: Hysteresis loop of **ole-pen/w-1/2-180** at 10, 300 K.

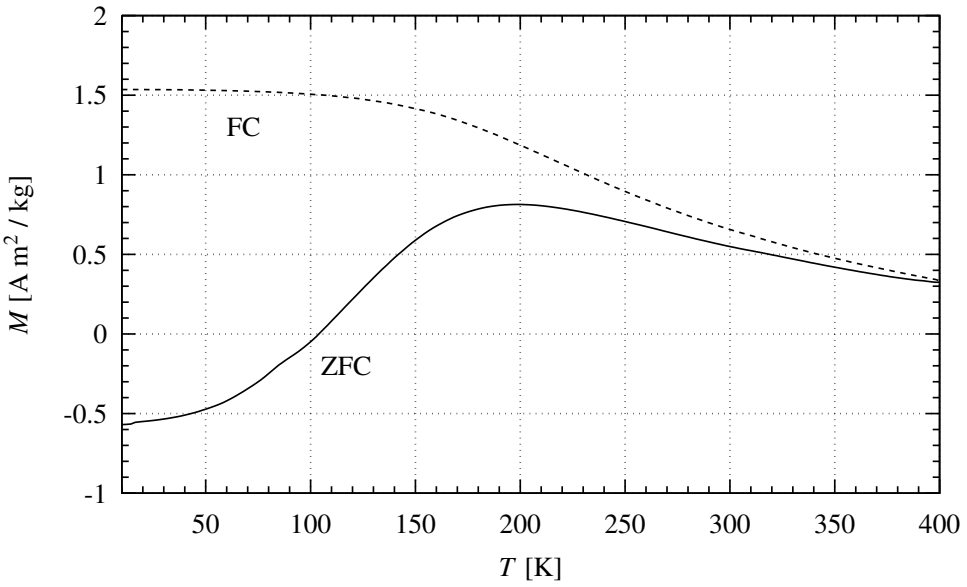

Figure 5.16: ZFC-FC measurement of sample **ole-pen/w-1/2-180+DMSA** at 5 mT.

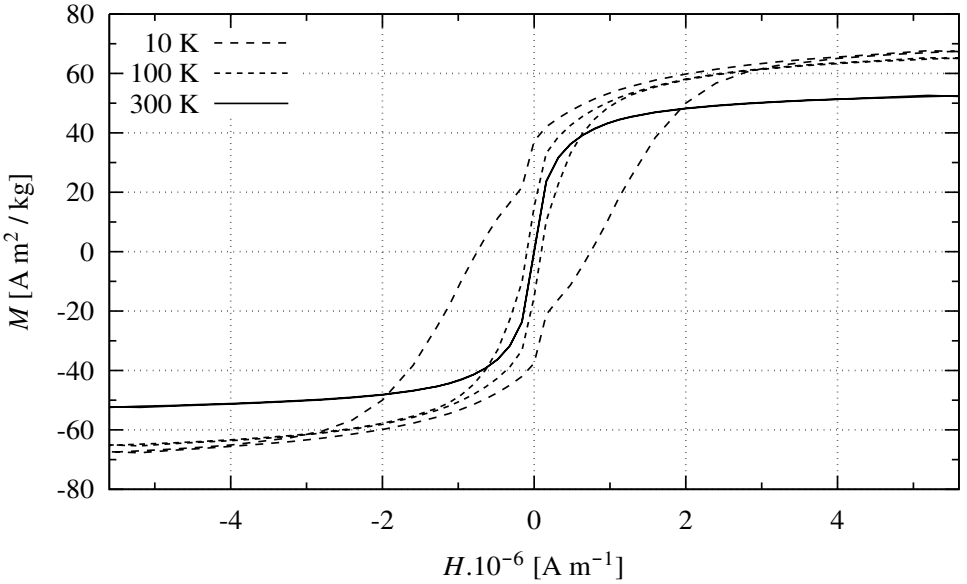

Figure 5.17: Hysteresis loop of **ole-pen/w-1/2-180+DMSA** at 10, 100, 300 K.

Sample ole-eth/w-2/1-180 was further investigated by Mössbauer spectroscopy. Clear sextets were found at 4 K and field 6 T (figure 5.19) and at field 0 T (figure 5.20). Results of fitting procedure are summarized in table 5.4. It shows, that iron ions are nearly statistically distributed in spinel structure, i.e. $Co_{0.33}Fe_{0.66}[Co_{0.66}Fe_{1.33}O_4]$. At room temperature, only very weak singlet (combined with siglet of Fe^0; figure 5.18) was found, with 0.5% intensity compared to sextets at 4 K. Calculation shows, that in one 6 nm particle, there are around 3000 atoms of Fe (16 Fe in $(8.39\ \text{Å})^3$ unit cell). Overall weight corresponds to 6000 atoms of Fe. Momentum carried by particle after photon absorption (see 3.16) would be $\Delta E_{\text{free}}/6000 \approx 2.3 \cdot 10^{-11} E_\gamma$, which is far more than the width of photon energy distribution $\Gamma = 3.2 \cdot 10^{-13} E_\gamma$. Particles have flexible oleic acid molecules on their surface, which facilitate their movement, so resonant absorption at room temperature is not possible.

Table 5.4: Analysis of Mössbauer spectrum of sample of $CoFe_2O_4$ nanoparticles **ole-eth/w-2/1-180** at 4 K. Bulk values reported for Fe^{3+} in magnetite are $\Delta E_Q = -0.02$, $\delta = 0.26$, $B = 49.0$ T [38]

	area	δ [mm/s]	ΔE_Q [mm/s]	B at 6 T	B at 0 T
sextet 1 (octahedral Fe^{3+})	68%	0.49	0.02	47.6 T	51.2 T
sextet 2 (tetrahedral Fe^{3+})	32%	0.37	-0.01	56.2 T	53.8 T

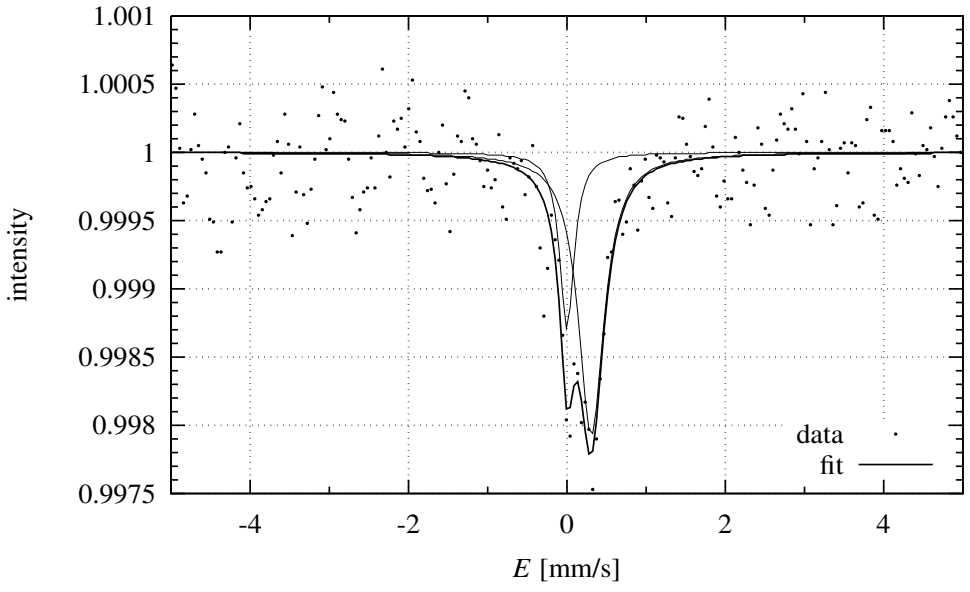

Figure 5.18: Mössbauer spectrum of **ole-eth/w-2/1-180** at 298 K.

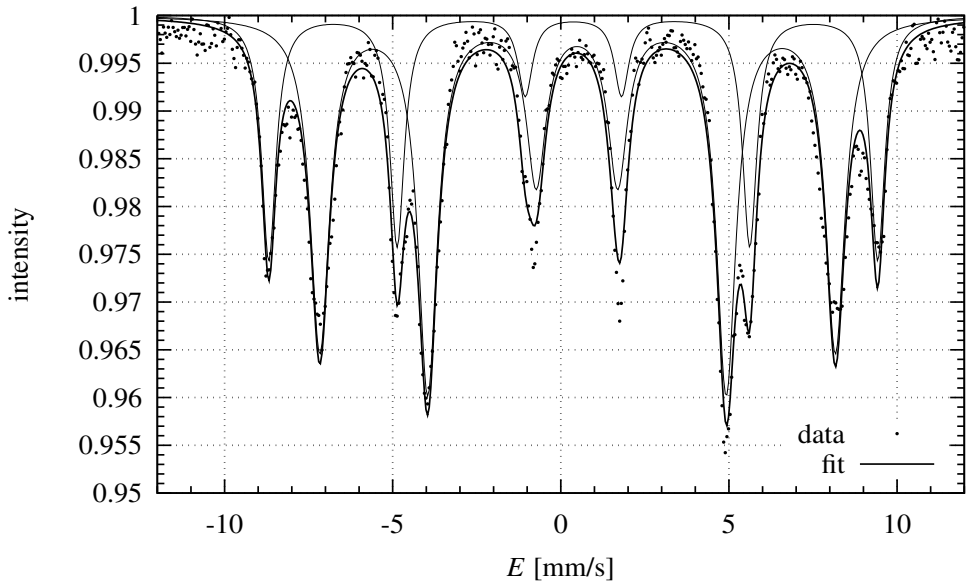

Figure 5.19: Mössbauer spectrum of sample **ole-eth/w-2/1-180** at 4 K and magnetic field 6 T.

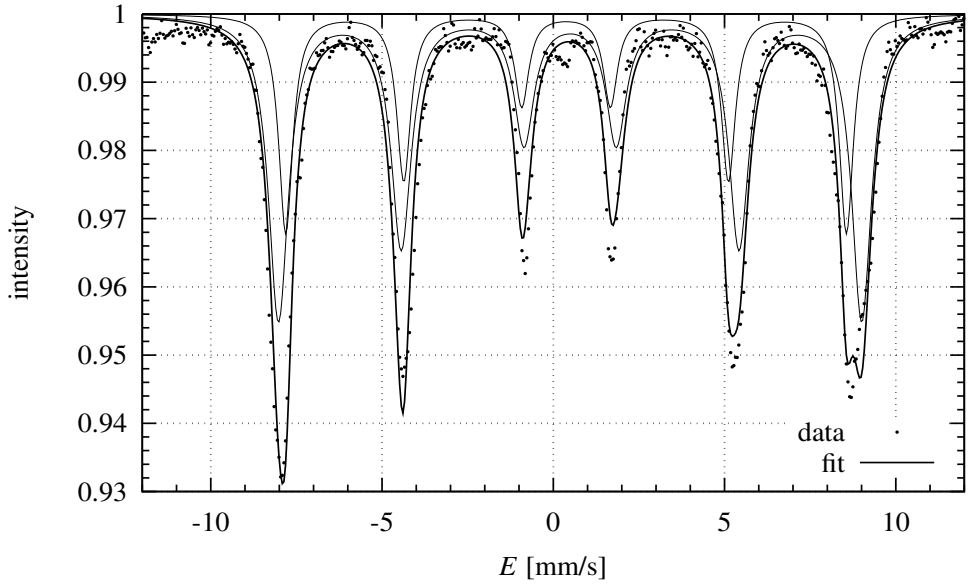

Figure 5.20: Mössbauer spectrum of sample **ole-eth/w-2/1-180** at 4 K and no magnetic field.

5.6 Up-conversion particles: size, structure and luminescence

Up-conversion particles were characterized by:

- Electron microscopy (TEM), figures 5.21, 5.22. Hexane dispersion (A) was diluted with hexane and a drop of it was dried on copper grid. Sediment (B) was dispersed in ethanol by sonication and a drop of it was dried on copper grid. Large particles were observed at magnification 10k or 15k, small particles at 100k or 150k.
- Powder X-ray diffraction with profile analysis, figures 5.23, 5.24.
- Up-conversion luminescence measurement at 980 nm excitation, table 5.5, figure 5.25.

Table 5.5: Relative intensities of up-conversion under 980 nm excitation for powder samples (B).

	λ [nm]	160 °C	180 °C	190 °C	200 °C	EDTA-4F	EDTA-8F
$NaYF_4$	539		1000	300	15	30	120
	654		500	200	40	50	30
LaF_3	539	0.008	7	0.3	0.07		
	654	0	3	0.2	0.08		

Y-EDTA-4F-200

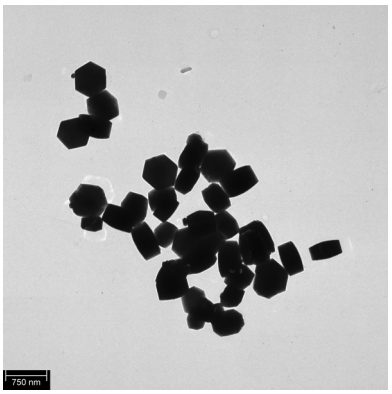

Y-EDTA-8F-200

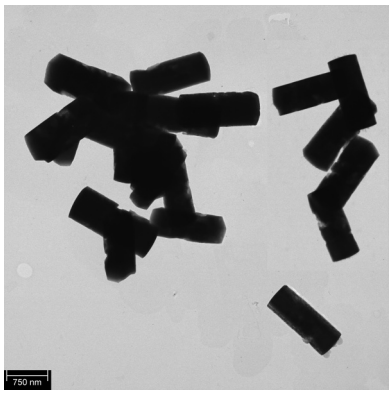

Figure 5.21: TEM figures of $NaYF_4$ prepared in ethanol - water - EDTA - oleylamine at Y:F 1:4 and 1:8. Magnification 1/2 compared to fig. 5.22 up.

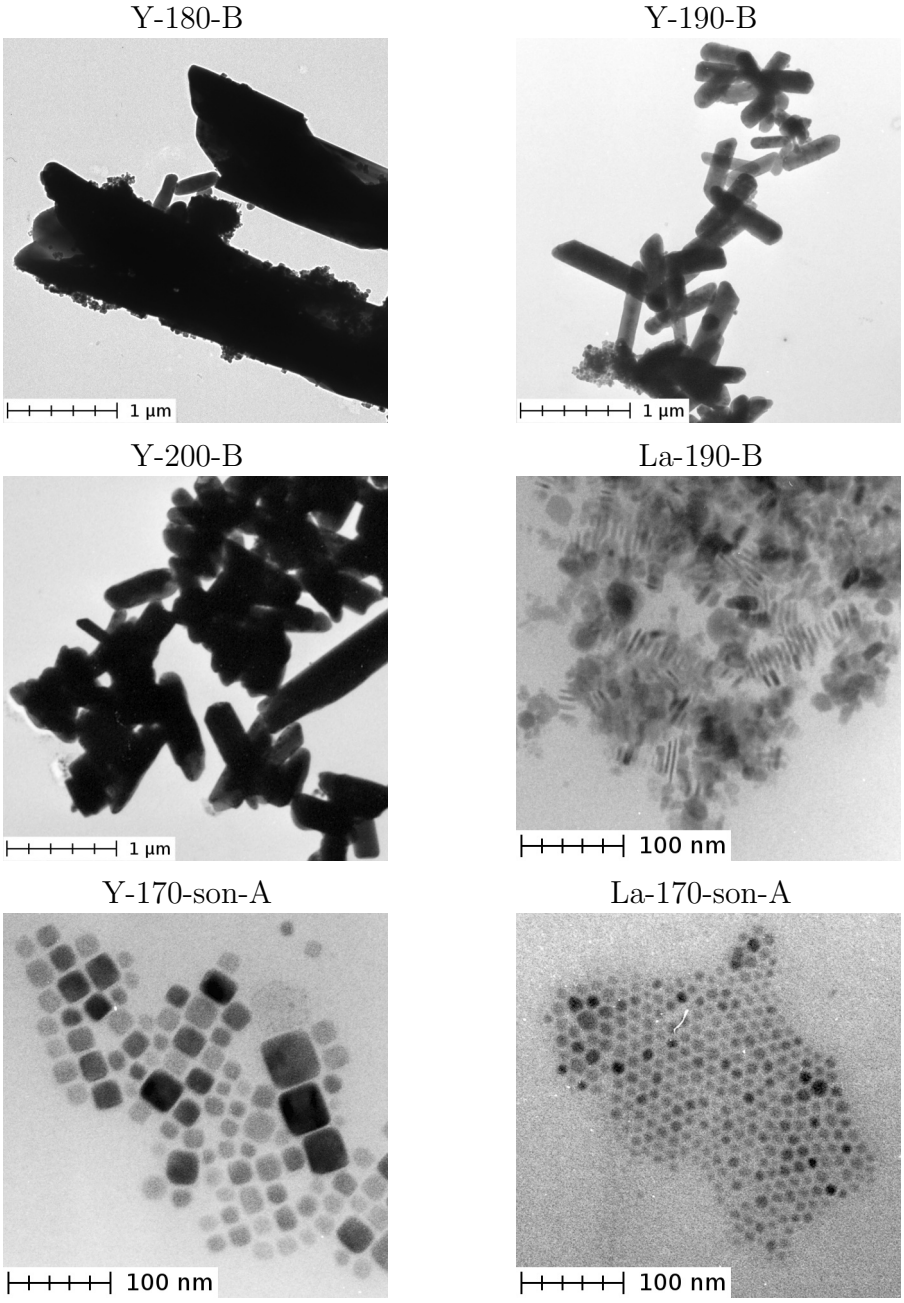

Figure 5.22: TEM figures of $NaYF_4$ and LaF_3. Upper pictures illustrate phase transformation of α-$NaYF_4$ (small spherical particles) into β-$NaYF_4$ (large rods). LaF_3 forms hexagonal plates seen either from top or side (**La-190-B**). **Y-170-son-A**: dispersible α-$NaYF_4$ cubes showing weak red up-conversion. **La-170-son-A**: nanoplates (by XRD) of LaF_3 with no up-conversion.

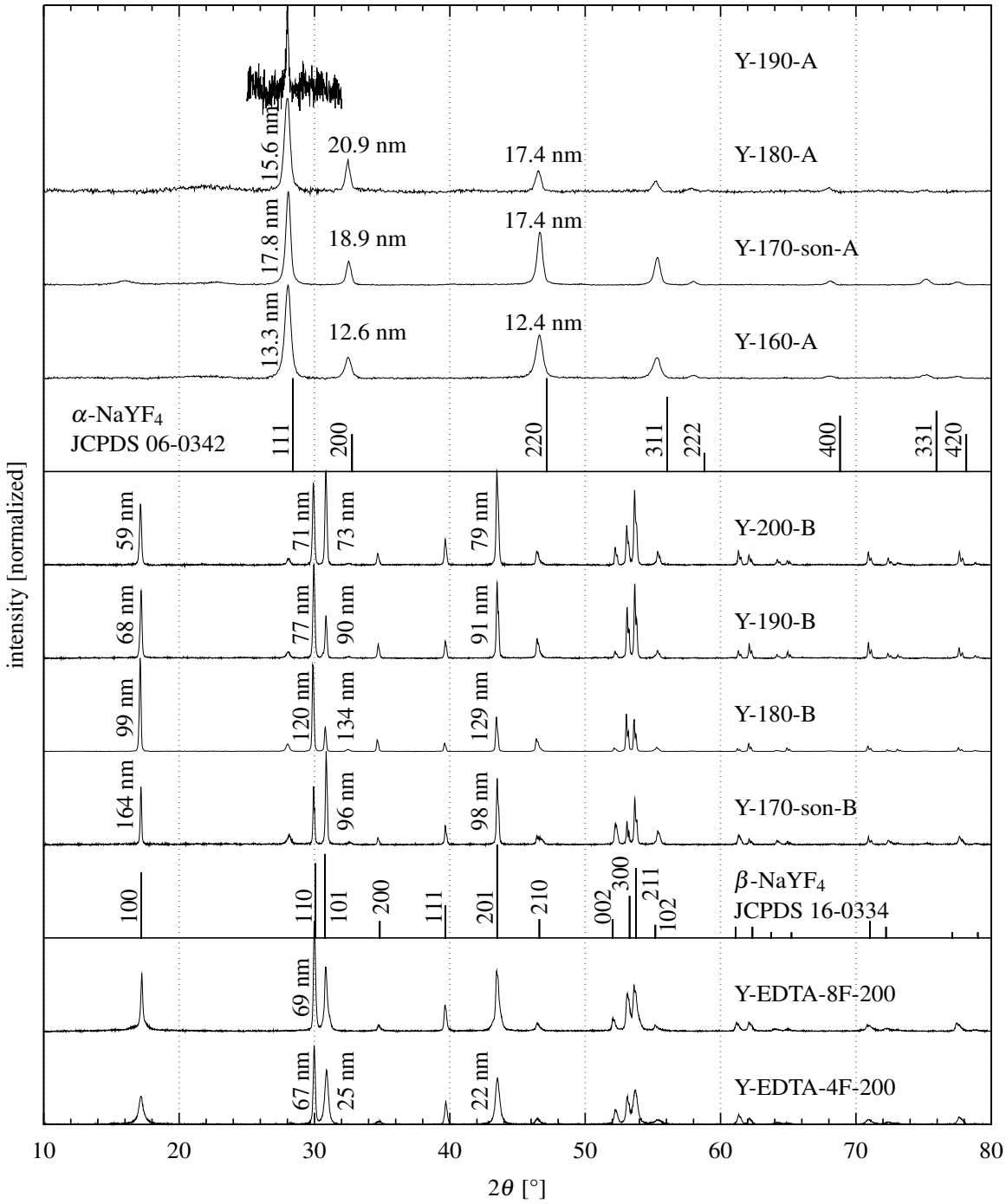

Figure 5.23: Powder X-ray diffraction of $NaYF_4$: Yb^{3+},Er^{3+} particles prepared at various temperatures: hexane dispersion (A) and sediment (B). Crystallite sizes obtained from profile analysis are given (> 50 nm values are understood as an estimate).

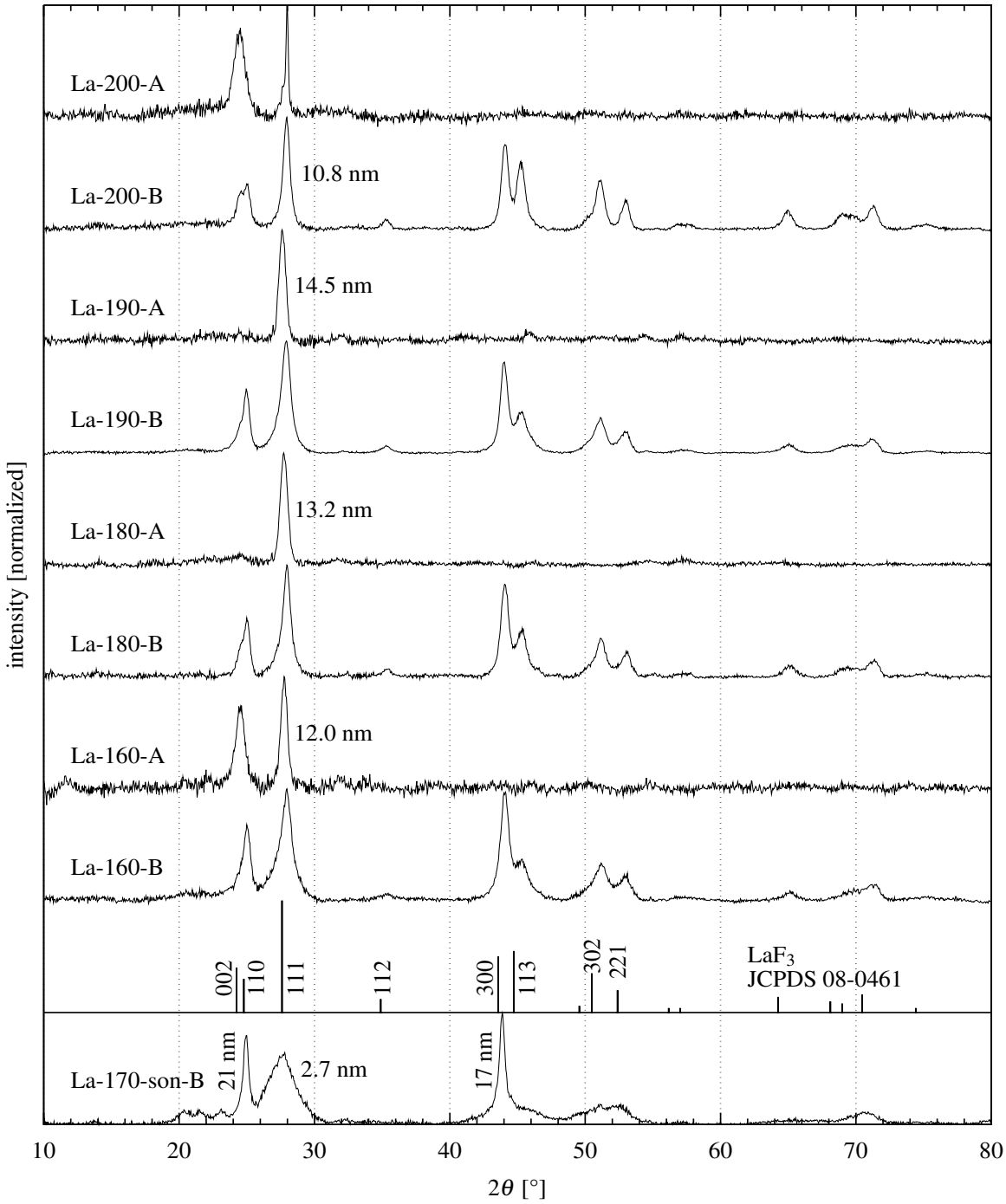

Figure 5.24: Powder X-ray diffraction of LaF_3: Yb^{3+},Er^{3+} particles prepared at various temperatures: hexane dispersion (A) and sediment (B). Crystallite sizes obtained from profile analysis are given.

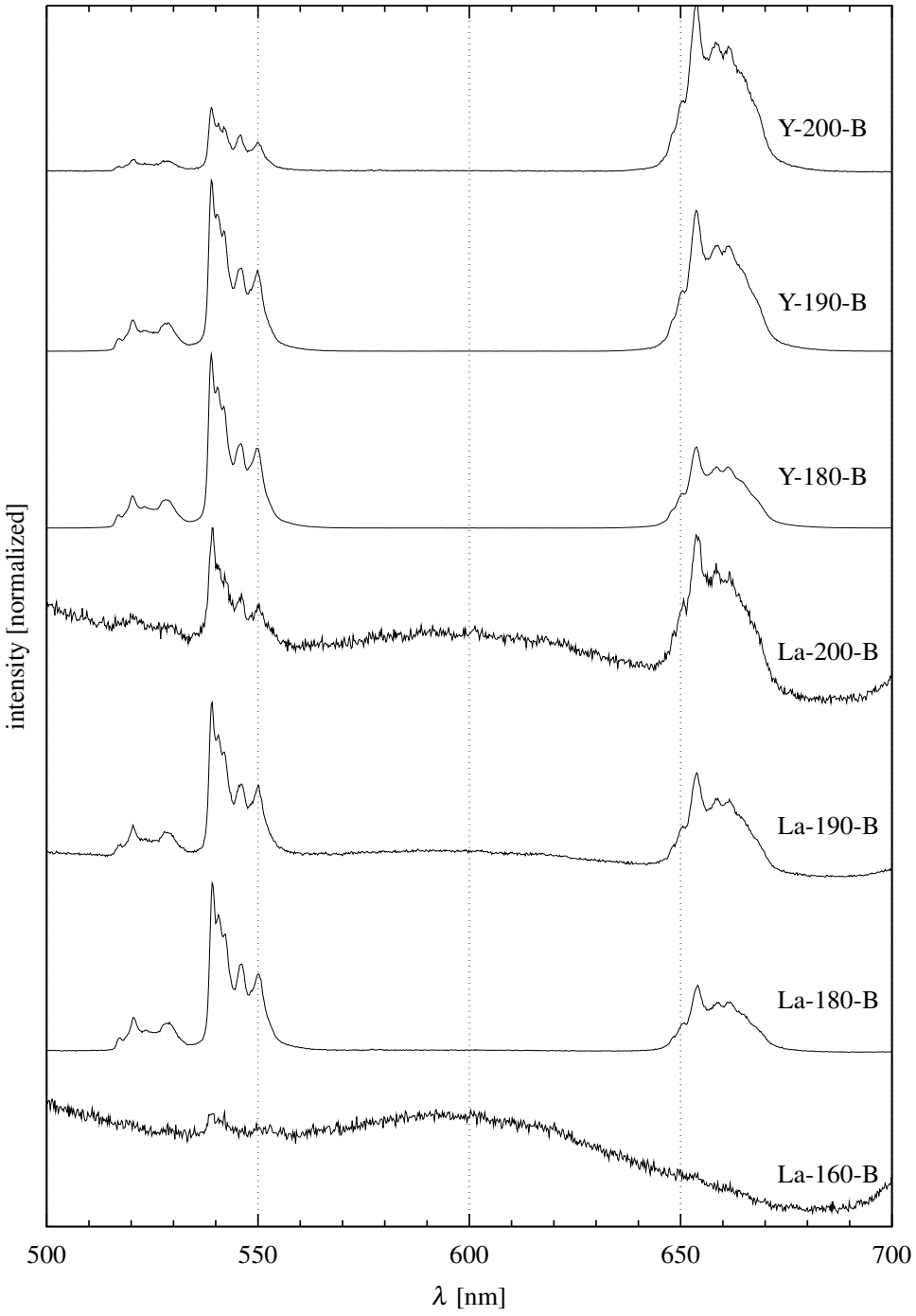

Figure 5.25: Up-conversion luminescence spectra of powder samples of $NaYF_4$: Er^{3+},Yb^{3+} and LaF_3: Er^{3+},Yb^{3+} under 980 nm excitation.

5.7 Discussion of up-conversion particles formation

There are many differences between hydrothermal synthesis of magnetic and up-conversion particles:

- Ln^{3+} and F^- react even at room temperature to form desired compounds (but not expected to be well crystalline).
- Although α-$NaYF_4$ (cubic, low up-conversion) is not thermodynamically preferred at temperatures < 700 °C, it is usually formed first due to kinetic reasons.
- After reaction at 160 °C only α-$NaYF_4$ dispersible in hexane was obtained and no β-$NaYF_4$, but after reaction at 200 °C β-$NaYF_4$ was obtained and almost no α-$NaYF_4$. There is a phase transformation from kinetically preferred α-$NaYF_4$ to thermodynamically stable β-$NaYF_4$. This tranformation is facilitated by high temperature and long time of hydrothermal treatment.
- β-$NaYF_4$ (hexagonal) was never found in hexane dispersion. Either oleic acid doesn't bond well to surface of β-$NaYF_4$ and is washed out, or recrystallization of β-$NaYF_4$ takes place in water, so there is no oleic acid on the surface of β-$NaYF_4$.

Following factors were found to correlate with up-conversion efficiency:

- β-$NaYF_4$ is much more efficient than α-$NaYF_4$.
- Larger crystals of α- and β-$NaYF_4$ have higher efficiency. This was observed for Y-160, Y-170-son-A (α-$NaYF_4$; only qualitatively), Y-180, Y-190, Y-200 (β-$NaYF_4$) and Y-EDTA-4F-200, Y-EDTA-8F-200 (β-$NaYF_4$). Particle sizes (as lower bounds) were determined by X-ray diffraction (figure 5.23), but for larger particles they are only rough estimates. TEM pictures show much larger particles (figures 5.21, 5.22)
- Intensity ratio of (110) and (101) diffraction. Higher efficiency correlates with lower intensity of (101) – this can be explained either by preferential orientation (more prolongated rods) or by cation distribution in lattice.

- When using EDTA, diffraction peaks (at figure 5.23 bottom) don't have expected profiles (there were problems with fitting procedure) and are much broader than expected from TEM measurements (figure 5.22). This can be explained by separation of Y^{3+} and Yb^{3+} by EDTA, and by subsequent lattice parameters variation – this also explains lower up-conversion efficiency of EDTA samples.

- Sonication of reaction mixtures before hydrothermal treatment. When sonication was done, efficiency of up-conversion was very low, in the order of LaF_3 efficiency. It is possible that without previous sonication, precursors react only at high temperature, and β-$NaYF_4$ is formed directly. However, this no-mixing approach is not expected to be well reproducible, so other routes will be investigated. It is interesting, that similar precursor separation was employed also in other reported procedures: liquid $Ln(oleate)_3$ in octadecene with solid NaF [21, 23] or hydrothermaly treated solid $Ln(stearate)_3$ and NaF in water-ethanol-polymer solution [27].

Interesting observation could be made on XRD of La-170-son-B sample (figure 5.24). Hexagonal plates are apparenly very thin, so diffraction peaks are broad. But peaks corresponding to planes perpendicular to surface of plates, $(hk0)$ are narrow – corresponding to low height/width ratio of nanoplates.

From observed facts, it can be concluded, that if we want to obtain β-$NaYF_4$ particles dispersible in hexane, recrystallization should be made in entirely organic media to retain oleic acid on the surface of particles (e.g. toluene under pressure, as was done for $CoFe_2O_4$). Other possiblity would be to prepare directly hydrophilic particles in water, but this method never led to particles smaller than 40 nm (see Literature review). Or use Gd^{3+} as dopant and modify composition of reaction mixture to obtain spherical or shorter rod-like particles, e.g. by changing Ln^{3+}:F^- ratio (particles prepared in [5] had rod shape with high height/width ratio).

Chapter 6

Summary

Hydrothermal synthesis in oleic acid - sodium oleate - water - pentanol was succesfully applied to preparation of high-quality cobalt ferrite nanoparticles with diameter (5.8 ± 1.1) nm ($w = 0.19$) covered with oleic anions (25% by weight) and readily dispersible in non-polar solvents. Dependence of particle properties on the variations in composition of reaction mixture was investigated and the mechanism of particle formation was proposed. Prepared particles were characterized by TEM, elemental analysis, thermogravimetry, powder X-ray diffraction, dynamic light scattering and magnetic measurements. They were superparamagnetic at room temperature, and showed good magnetic properties at 10 K: coercivity 1.16 T and saturation magnetization 68 $A.m^2.kg^{-1}$. Based partially on suggested mechanism of particle formation, novel route was proposed: decomposition of metal oleates in toluene under pressure in the presence of water. It led to the particles of equally good properties as in the previous case.

Magnetic particles were further modified by dimercaptosuccinic acid. Particles were then treated with well-defined amount of NaOH, what facilitated creation of stable water dispersion with the hydrodynamic diameter of particles as low as 20 nm, and stable against agglomeration down to pH 3. Magnetic properties were retained, but indication of stronger inter-particle interaction was found.

Particles of $NaYF_4$ and LaF_3 showing up-conversion luminescence were prepared. Phase transition behaviour of $NaYF_4$ was investigated, but preparation of small (< 100 nm) β-$NaYF_4$ particles (the most efficient up-conversion material) was not succesful so far. It will be neccesary to try other approaches based on recent proposals in literature.

Abbreviations

CGS	centimeter, gram, second (old unit system)
DLS	dynamic light scattering
DMSA	meso-2,3-dimercaptosuccinic acid
DMSO	dimethyl sulfoxide
DTA	differential thermal analysis
EDTA	ethylenediaminetetraacetic acid
FTIR	Fourier transform infrared spectroscopy
ICP-AES	inductively coupled plasma atomic emission spectroscopy
L-S	coupling of orbital and spin momentum in atoms and ions
NIR	near infrared
PDI	polydispersity index
SI	Système international d'unités, International System of Units
TEM	transmission electron microscopy
TG	thermogravimetry
XRD	(powder) X-ray diffraction

Bibliography

[1] S. Sun, H. Zeng, D. B. Robinson, S. Raoux, P. M. Rice, S. X. Wang, G. Li: Monodisperse MFe_2O_4 (M = Fe, Co, Mn) nanoparticles. *Journal of American Chemical Society* **126** (2004) 273–279.

[2] X. Wang, J. Zhuang, Q. Peng, Y. Li: A general strategy for nanocrystal synthesis. *Nature* **437** (2005) 121–124.

[3] N. Menyuk, K. Dwight, J. W. Pierce: $NaYF_4$: Yb,Er – an efficient upconversion phosphor. *Applied Physics Letters* **21** (1972) 159–161.

[4] F. Wang, X. Liu: Recent advances in the chemistry of lanthanide-doped upconversion nanocrystals. *Chemical Society Reviews* **38** (2009) 976–989.

[5] F. Wang, Y. Han, C. S. Lim, Y. Lu, J. Wang, J. Xu, H. Chen, C. Zhang, M. Hong, X. Liu: Simultaneous phase and size control of upconversion nanocrystals through lanthanide doping. *Nature* **463** (2010) 1061–1065.

[6] N. Bao, L. Shen, W. An, P. Padhan, C. H. Turner, A. Gupta: Formation mechanism and shape control of monodisperse magnetic $CoFe_2O_4$ nanocrystals. *Chemistry of Materials* **21** (2009) 3458–3468.

[7] X. Liang, X. Wang, J. Zhuang, Y. Chen, D. Wang, Y. Li: Synthesis of nearly monodisperse iron oxide and oxyhydroxide nanocrystals. *Advanced Functional Materials* **16** (2006) 1805–1813.

[8] A. G. Roca, S. Veintemillas-Verdaguer, M. Port, C. Robic, C. J. Serna, M. P. Morales: Effect of nanoparticle and aggregate size on the relaxometric properties of MR contrast agents based on high quality magnetite nanoparticles. *Journal of Physical Chemistry B* **113** (2009) 7033–7039.

[9] C. B. Murray, D. J. Norris, M. G. Bawendi: Synthesis and characterization of nearly monodisperse CdE (E = S, Se, Te) semiconductor nanocrystallites. *Journal of American Chemical Society* **115** (1993) 8706–8715.

[10] J. P. Ge, S. Xu, J. Zhuang, X. Wang, Q. Peng, Y. D. Li: Synthesis of CdSe, ZnSe, and ZnCdSe nanocrystals and their silica sheathed core/shell structures. *Inorganic Chemistry* **45** (2006) 4922–4927.

[11] M. D. Mathews, B. R. Ambekar, A. K. Tyagi, J. Köhler: High temperature X-ray diffraction studies on sodium yttrium fluoride. *Journal of Alloys and Compounds* **377** (2004) 162–166.

[12] K. W. Krämer, D. Biner, G. Frei, H. U. Güdel, M. P. Hehlen, S. R. Lüthi: Hexagonal sodium yttrium fluoride based green and blue emitting upconversion phosphors. *Chemistry of Materials* **16** (2004) 1244–1251.

[13] Y. W. Zhang, X. Sun, R. Si, L. P. You, C. H. Yan: Single-crystalline and monodisperse LaF_3 triangular nanoplates from a single-source precursor. *Journal of American Chemical Society* **127** (2005) 3260–3261.

[14] H. Hu, Z. Chen, T. Cao, Q. Zhang, M. Yu, F. Li, T. Yi, C. Huang: Hydrothermal synthesis of hexagonal lanthanide-doped LaF_3 nanoplates with bright upconversion luminescence. *Nanotechnology* **19** (2008) 375702 (9pp).

[15] G. S. Yi, G. M. Chow: Synthesis of hexagonal-phase $NaYF_4$:Yb,Er and $NaYF_4$:Yb,Tm nanocrystals with efficient up-conversion fluorescence. *Advanced Functional Materials* **16** (2006) 2324–2329.

[16] H. X. Mai, Y. W. Zhang, R. Si, Z. G. Yan, L. D. Sun, L. P. You, C. H. Yan: High-quality sodium rare-earth fluoride nanocrystals: controlled synthesis and optical properties. *Journal of American Chemical Society* **128** (2006) 6426–6436.

[17] J. C. Boyer, F. Vetrone, L. A. Cuccia, J. A. Capobianco: Synthesis of colloidal upconverting $NaYF_4$ nanocrystals doped with Er^{3+}, Yb^{3+} and Tm^{3+}, Yb^{3+} via thermal decomposition of lanthanide trifluoroacetate precursors. *Journal of American Chemical Society* **128** (2006) 7444–7445.

[18] H. X. Mai, Y. W. Zhang, L. D. Sun, C. H. Yan: Size- and phase-controlled synthesis of monodisperse $NaYF_4$:Yb,Er nanocrystals from a unique delayed nucleation pathway monitored with upconversion spectroscopy. *Jornal of Physical Chemistry C* **111** (2007) 13730–13739.

[19] G. S. Yi, G. M. Chow: Water-soluble $NaYF_4$:Yb,Er(Tm)/ $NaYF_4$/polymer core/shell/shell nanoparticles with significant enhancement of upconversion fluorescence. *Chemistry of Materials* **19** (2007) 341–343.

[20] L. P. Qian, D. Yuan, G. S. Yi, G. M. Chow: Critical shell thickness and emission enhancement of $NaYF_4$:Yb,Er/$NaYF_4$/silica core/shell/shell nanoparticles. *Journal of Materials Research* **24** (2009) 3559–3568.

[21] Y. Wei, F. Lu, X. Zhang, D. Chen: Synthesis of oil-dispersible hexagonal-phase and hexagonal-shaped $NaYF_4$:Yb,Er nanoplates. *Chemistry of Materials* **18** (2006) 5733–5737.

[22] Z. Li, Y. Zhang: An efficient and user-friendly method for the synthesis of hexagonal-phase $NaYF_4$:Yb, Er/Tm nanocrystals with controllable shape and upconversion fluorescence. *Nanotechnology* **19** (2008) 345606 (5pp).

[23] C. Liu, H. Wang, X. Li, D. Chen: Monodisperse, size-tunable and highly efficient β-$NaYF_4$:Yb,Er(Tm) up-conversion luminescent nanospheres: controllable synthesis and their surface modifications. *Journal of Materials Chemistry* **19** (2009) 3546–3553.

[24] H. Schäfer, P. Ptacek, H. Eickmeier, M. Haase: Synthesis of hexagonal Yb^{3+}, Er^{3+}-doped $NaYF_4$ nanocrystals at low temperature. *Advanced Functional Materials* **19** (2009) 3091–3097.

[25] L. Wang, Y. Li: Controlled synthesis and luminescence of lanthanide doped $NaYF_4$ nanocrystals. *Chemistry of Materials* **19** (2007) 727–734.

[26] F. Zhang, J. Li, J. Shan, L. Xu, D. Zhao: Shape, size, and phase-controlled rare-earth fluoride nanocrystals with optical up-conversion properties. *Chemistry – A European Journal* **15** (2009) 11010–11019.

[27] M. Wang, C. C. Mi, J. L. Liu, X. L. Wu, Y. X. Zhang, W. Hou, F. Li, S. K. Xu: One-step synthesis and characterization of water-soluble

$NaYF_4$:Yb,Er/polymer nanoparticles with efficient up-conversion fluorescence. *Journal of Alloys and Compounds* **485** (2009) L24–L27.

[28] J. H. Zeng, J. Su, Z. H. Li, R. X. Yan, Y. D. Li: Synthesis and upconversion luminescence of hexagonal-phase $NaYF_4$: Yb,Er^{3+} phosphors of controlled size and morphology. *Advanced Materials* **17** (2005) 2119–2123.

[29] L. Wang, R. Yan, Z. Huo, L. Wang, J. Zeng, J. Bao, X. Wang, Q. Peng, Y. Li: Fluorescence resonant energy transfer biosensor based on upconversion-luminescent nanoparticles. *Angewandte Chemie International Edition* **44** (2005) 6054–6057.

[30] X. Liu, J. Zhao, Y. Sun, K. Song, Y. Yu, C. Du, X. Kong, H. Zhang: Ionothermal synthesis of hexagonal-phase $NaYF_4$:Yb^{3+},Er^{3+}/Tm^{3+} upconversion nanophosphors. *Chemical Communications* (2009) 6628–6630.

[31] X. Yu, M. Li, M. Xie, L. Chen, Y. Li, Q. Wang: Dopant-controlled synthesis of water-soluble hexagonal $NaYF_4$ nanorods with efficient upconversion fluorescence for multicolor bioimaging. *Nano Research* **3** (2010) 51–60.

[32] H. Ahlers, J. Sievert: *Units in Physics and Chemistry, Sect. 2.3.3.2 Polarization*, Landolt-Börnstein (Springer, Berlin Heidelberg New York 1991), 2–285 – 2-294; URL (28.4.2010): `http://smart.springer.de/licensed_materials/0284/tocs/000/t000_units_a0288.pdf`

[33] C. Kittel: *Introduction to Solid State Physics*, 7th edition (Wiley 1996).

[34] T. Mayer-Kuckuk: *Fyzika atomového jádra* (SNTL Praha, 1979); translation of T. Mayer-Kuckuk: *Physik der Atomkerne* (B. G. Teubner Stuttgart, 1974).

[35] C. Liu, B. Zou, A. J. Rondinone, Z. J. Zhang: Chemical control of superparamagnetic properties of magnesium and cobalt spinel ferrite nanoparticles through atomic level magnetic couplings. *Journal of American Chemical Society* **122** (2000) 6263–6267.

[36] J. J. Lu, H. Y. Deng, H. L. Huang: Thermal relaxation of interacting fine magnetic particles – field-cooled and zero-field-cooled magnetization variation. *Journal of Magnetism and Magnetic Materials* **209** (2000) 37–41.

[37] LBNL Isotopes Project, Berkeley, USA (`http://ie.lbl.gov/toi.html`; retrieved 26.4.2010).

[38] E. Murad, J. H. Johnston: Iron Oxides and Hydroxides, in: *Mössbauer Spectroscopy Applied to Inorganic Chemistry* **2** (Plenum Press, New York, 1987) 507–583.

[39] *Zetasizer Nano Series: User Manual*, issue 2.2 (Malvern Instruments Ltd. 2005).

[40] F. Auzel: Upconversion and anti-Stokes processes with f and d ions in solids. *Chemical Reviews* **104** (2004) 139–173.

[41] W. F. Krupke: Energy levels of Er^{3+} in LaF_3 and coherent emission at 1.61 μ. *The Journal of Chemical Physics* **41** (1964) 1225–1232.

[42] W. T. Carnall, P. R. Fields, J. Morrison, R. Sarup: Absorption spectrum of Tm^{3+}:LaF_3. *The Journal of Chemical Physics* **52** (1970) 4054–4059.

[43] H. E. Rast, H. H. Caspers, S. A. Miller: Fluorescence and energy transfer between Nd^{3+} and Yb^{3+} in LaF_3. *The Journal of Chemical Physics* **47** (1967) 3874–3878.

[44] J. F. Suyver, J. Grimm, K. W. Krämer, H. U. Güdel: Highly efficient near-infrared to visible up-conversion process in $NaYF_4$: Er^{3+}, Yb^{3+}. *Journal of Luminescence* **114** (2005) 53–59.

[45] W. H. Zachariasen: The UCl_3 type of crystal structure. *The Journal of Chemical Physics* **16** (1948) 254.

[46] A. Grzechnik, P. Bouvier, M. Mezouar, M. D. Mathews, A. K. Tyagi, J. Köhler: Hexagonal $Na_{1.5}Y_{1.5}F_6$ at high pressures. *Journal of Solid State Chemistry* **165** (2002) 159–164.

[47] J. A. Dean: *Lange's Handbook of Chemistry*, 15th edition (McGRAW-HILL, 1999).

[48] V. Blaskov, V. Petkov, V. Rusanov, L. M. Martinez, B. Martinez, J. S. Muñoz, M. Mikhov: Magnetic properties of nanophase $CoFe_2O_4$ particles. *Journal of Magnetism and Magnetic Materials* **162** (1996) 331–337.